

Relating Micro-segregation to Site Specific High Temperature Deformation in Single Crystal Nickel-base Superalloy Castings

Neil D'Souza¹, Bryan Roebuck², David M. Collins³, Geoff D. West⁴, Chinnapat Panwisawas^{5,*}

¹Rolls-Royce plc, PO Box 31, Derby, DE24 8BJ, United Kingdom

²National Physical Laboratory, Hampton Road, Teddington, Middlesex, TW11 0LW, United Kingdom

³School of Metallurgy and Materials, University of Birmingham, Birmingham B15 2TT, United Kingdom

⁴Warwick Manufacturing Group, University of Warwick, Coventry CV4 7AL, United Kingdom

⁵Department of Materials, University of Oxford, Parks Road, Oxford OX1 3PH, United Kingdom

**Corresponding author: chinnapat.panwisawas@materials.ox.ac.uk*

Abstract

Thermo-mechanical deformation of the solid on cooling following solidification has been studied quantitatively in a Ni-base single crystal superalloy, CMSX4 used in turbine blade applications. In the as-cast state, the alloy has location specific properties due to micro-segregation of alloying elements during solidification; this effect become increasingly important with smaller specimen cross-section in thermo-mechanical tests. Accordingly, normalised resistance/resistivity tests have been used to classify samples with varying micro-segregation, given the different γ and γ' phase resistivities. Increased normalised resistance corresponds to increased local solvus temperature, which determines the plastic strain and stress evolution during cooling. Upon cooling from above the γ' solvus temperature, dislocation creep occurs within the γ phase accompanied by a small increase in stress. A critical precipitation γ' volume fraction is reached as the material cools, leading to precipitation hardening as measured by a dramatic resistance change and thereby stress increase at lower temperatures. Short-term creep tests capturing the history-dependent deformation, as demonstrated by controlled cooling experiments, gives steady-state creep, enabling parameter measurement for a Norton-type constitutive equation in a given temperature range. Implications of these results to modelling of plastic strain and stress during cooling from close to solvus temperature during casting has been discussed.

1. Introduction

One of the principal defects in single crystal nickel-based superalloy investment cast turbine blades is secondary grains. The alloys used for these components do not contain grain boundary strengthening alloying elements, giving a dramatic drop in strength at high temperatures when secondary grains occur. Of this class of secondary grains, one constitutes recrystallisation. This is defined by the formation of equiaxed grains following solution heat treatment, which is required to eliminate as-cast eutectic phases and to attain of compositional homogeneity. Thermo-mechanical deformation following solidification progressively occurs in the solid, which is dependent on the cooling rate and specific geometrical features in the casting. The latter comprises regions of small radii of curvature, associated with fillet radii in turbine blades, where stress concentration features will lead to plasticity, providing a driving sufficient to trigger re-crystallisation on heat treatment [1]. Therefore, it is important to calculate the evolution of plastic strain and stress response during cooling for predicting such defects using numerical modelling. This in turn requires detailed experimentation for obtaining reliable time-dependent thermo-mechanical deformation data at high temperature.

Traditionally, experimental approaches have involved use of isothermal stress-strain curves under constant strain rate or stress to describe the constitutive material behaviour [2 - 5]. However, non-isothermal creep properties under such high temperature/low strain (strain rate) conditions have also been extensively studied in Ni-base superalloys [6 - 9]. The time duration of such tests is typically greater than 50 hours; this is therefore unrepresentative of the less than 1-hour casting process. Furthermore, such creep tests do not capture the history dependent deformation during casting. In casting, this history-dependence is considered to be important as deformation at higher temperature is expected to play a key role in the subsequent deformation induced at lower temperature; an aspect missing in the tests representative of in-service conditions. Another aspect that is missing in these studies is specifically the role of micro-segregation, which is characteristic of the as-cast state, but absent in the homogenised condition. Micro-segregation arises because of difference in solute solubility in the solid and liquid and resulting in solute partitioning. Micro-segregation is further exacerbated when solid-state diffusion is limited, specifically in the case of refractory alloying additions, such as Ta, W and Re, which is characteristic of 2nd and 3rd generation Ni-base alloys [10]. The solidification path is dependent on micro-segregation and will determine the amount of non-equilibrium phases that occur with the inter-dendritic region [11]. In the presence of such non-equilibrium (eutectic) phases, it has been shown that deformation is concentrated near this eutectic morphology. The accumulated plastic strain subsequently promotes re-crystallisation during subsequent solutioning to eliminate micro-segregation [12, 13]. This is additionally confirmed by other studies, which report that dendrite cores (segregated in W and Re) which are the regions that solidify first are virtually dislocation free. In the inter-dendritic region across the dendrite cross-section, there is an increase in dislocation density, observed as loops around precipitates [14].

Therefore, the quantification of time-dependent deformation during deformation has been carried out using two different approaches;

- ‘*In-situ*’ measurements exploring various boundary conditions have been made to replicate manufacturing conditions. This has included cooling under different conditions, i.e. strain or displacement control, with lattice (elastic) strain measured using neutron diffraction techniques [15, 16]. This method enables the elastic behaviour of the major phases; the γ matrix and γ' strengthening precipitates, to be independently characterised, where dislocation-hardening behaviour may be inferred from lattice strain evolution. However, weak superlattice reflections associated with the γ' phase make accurate quantification of dislocation densities from peak broadening analysis highly inaccurate. Furthermore, experiments are limited to slow cooling rates due to neutron signal acquisition times. These drawbacks do not exist for experiments at constant temperature and/or longer dwell times, such as creep and stress relaxation in similar alloys [17, 18]. Finally, studies requiring access to high temperature furnaces are complex as a number of experimental issues need to be overcome; this includes oxidation & corrosion effects, suitable sample monitoring including specialised thermocouples & strain gauges as well as thermal scattering associated signal attenuation effects. These effects are relevant here as plastic strain that induces re-crystallisation occurs above 1000°C [1, 14].
- ‘*Post-mortem*’ experiments to study recrystallisation have also been performed. In such studies, laboratory load frames are used at high temperature to subject samples to tensile/creep/stress relaxation test conditions to determine the temperature-dependent flow stress. However, tensile gripping is limited to a maximum temperature of 1150°C [2, 14]. This may be overcome by using compressive loading with flat platens, (e.g. using a Gleeble [19, 20]). However, the effect of compression instead of tension induced recrystallisation has not been verified.

Therefore, in order to overcome the major limitation in maximum temperature possible using existing techniques to enable the measurement of flow stress and creep strain from 1300°C, which is close to the solvus temperature, an alternative experimental method is required. A unique method to overcome these issues is to use electro-thermal miniature testing (ETMT). In addition to tensile testing (replicating a conventional uniaxial load frame), elevated temperature testing is possible by passing a resistive current through electrically conductive samples. Water-cooled grips are used to give a temperature gradient along the length of the sample [21, 22]. Recent studies have confirmed that at a central temperature up to around 900°C, the temperature distribution along the test-piece is parabolic [23, 24]. Consequently, the temperature variation along the 3 mm gauge length for Ni-base alloys is typically 5°C [25]. At temperatures approaching 1300°C, radiation losses become more important and resulting in a smaller temperature variation within the central gauge length. Consequently, a small gauge volume with a tight control of temperature permits accurate measurement of plastic strain through measurement of sample resistance [21, 22].

Thermo-mechanical data generated may be used to calculate plastic strain and stress that develops within a casting during cooling. Accordingly, thermo-elasto-plastic models may be employed. These models implicitly assume a constitutive law where stress is a function of time-dependent plastic strain rate, plastic strain and

temperature [14, 26, 27]. Consequently, the high fidelity thermo-mechanical data measured in this study by overcoming the drawbacks in *in-situ* or *post-mortem* approaches can be used in a numerical model, where the issues of history-dependent deformation are addressed by building on a previous study [28]. Therefore, the objectives in this study are two-fold;

- (i) To carry out cooling experiments under displacement control to obtain a range of plastic strains as in [14], which is typical of casting conditions. The evolution of stress, is then used to dictate the subsequent flow stress and creep experiments.
- (ii) To carry out flow stress and short-term creep tests that appropriately incorporates the history-dependence of prior deformation, which is described in the experimental section. A constitutive equation for creep is then derived from this data.

2. Experimental Method

2.1 Materials

Single crystal test bars from the Ni-base superalloy, CMSX-4 with nominal composition given in Table 1, were directionally solidified and with axial orientations within 10° from $\langle 001 \rangle$. Cylindrical samples had ~ 10 mm diameter and ~ 60 mm length. Apart from as-cast test bars, one of these was solutioned (heat treated) at a nominal temperature of 1310°C for 6 hours to dissolve the as-cast eutectic and homogenise the segregated as-cast microstructure. Test-pieces were electro-discharge machined (EDM) from the test bars to have a slightly larger than nominal $2\text{ mm} \times 1\text{ mm}$ and $2\text{ mm} \times 2\text{ mm}$ cross section along the full length (40 mm). The EDM surfaces were ground with abrasive media to remove any re-cast EDM layer and surface residual stresses. Test specimens were cuboids; $2\text{ mm} \times 1\text{ mm} \times 40\text{ mm}$ and in some cases; $2\text{ mm} \times 2\text{ mm} \times 40\text{ mm}$.

2.2 Electro-thermal Miniature Testing (ETMT)

2.2.1 Plastic Strain Measurement

The resistance is initially calculated at room temperature (RT) by measuring the specimen current (I) after application of a fixed potential difference ($V \sim 1.6\text{ mV}$ or $\sim 3.2\text{ mV}$) between two points; $L = 4.2\text{ mm}$ apart along the length of the sample. The resistance is calculated as; $R' = (V/I)$ and the resistivity is then calculated as; $\rho = R' (A/L)$, where A and L are the specimen cross section area ($2\text{ mm} \times 1\text{ mm}$) and length (4.2 mm) respectively. The calculated resistivity is typically in the range of $1.52 \times 10^{-9}\ \Omega\text{m}$ to $1.55 \times 10^{-9}\ \Omega\text{m}$ at room temperature. An ETMT system developed at the National Physical Laboratory was used to measure the macroscopic stress and plastic strain; the latter calculated by monitoring changes in resistance. More details of the experimental set-up can be obtained from [21 - 25]. From the measured resistivity (ρ) at RT as outlined above, the gauge length of the sample during testing under zero-load in the ETMT apparatus at RT can be then calculated as; $L_{\text{Gauge}} = R (A/\rho) \sim 2.75\text{ mm}$, where now R = measured resistance using ETMT and $A = 2\text{ mm} \times$

1 mm corresponding to the gauge length; L_{Gauge} This gauge length is almost constant during heating up to 1300°C under zero-load, since $\alpha\Delta T \sim 0.02 \ll 1$, where $\alpha = 15 \times 10^{-6} \text{ K}^{-1}$ [14, 27] and $\Delta T \sim 1300 \text{ }^\circ\text{C}$. Therefore, it is reasonable to approximate “constant gauge length under zero-load”. The gauge volume is therefore typically 5.5 – 11 mm³. The resolution of temperature measurement is determined by the type of thermocouple used, which in this case is Pt/Pt-13%Rh and is less than 1 °C at 1300°C. Within the central gauge length of the test piece the temperature profile is approximately uniform ($\pm 5 \text{ }^\circ\text{C}$). During cooling under zero-load from 1300°C to 1150°C in the ETMT, the change in resistance arises solely from change in resistivity, since gauge length and cross-section are almost constant, as explained above. The resistivity is a function of temperature (decreases with increasing temperature) as well as the phases present, since resistivity of $\gamma' >$ resistivity of γ . However, during cooling under displacement control, the change in resistance occurs from; (i) temperature and phase dependence (precipitation of γ') of resistivity, as determined using zero-load and (ii) from plastic deformation, since now both L and A change. The plastic strain, ε^{pl} , is given by

$$\varepsilon^{\text{pl}} = \ln\left(\frac{L_2}{L_1}\right) \quad (1)$$

where subscript 1 refers to the initial measured gauge length (under zero-load), and 2 is the strained gauge length, both at temperature, T. This can be related to the measured resistance, where $\rho = \frac{R_1 A_1}{L_1} = \frac{R_2 A_2}{L_2}$ and from the conservation of volume, $A_1 L_1 = A_2 L_2$, these expressions can be used to express Equation 1 as

$$\varepsilon^{\text{pl}} = \frac{1}{2} \ln\left(\frac{R_2}{R_1}\right) \quad (2)$$

Since the plastic strain is measured from the resistance, any error in the resistance measurement contributes to an error in the plastic strain. The current and voltage measurements are made with better than 1 part in 10⁴ uncertainty and the maximum range in the measured resistance is $\pm 0.002 \text{ m}\Omega$ and with an accompanying standard deviation of $\pm 0.001 \text{ m}\Omega$. From Equation 1, the upper and lower plastic bounds of plastic strains is given by; $\varepsilon^{\text{pl}} = \frac{1}{2} \ln\left(\frac{R \pm \Delta R}{R_0 \pm \Delta R_0}\right)$. This is used to estimate a plastic strain resolution of $\sim 0.05 \%$.

2.2.2 High Temperature Thermo-mechanical Testing

Three types of experiments were carried out using the ETMT method corresponding to; continuous cooling, flow stress and creep. In all cases, the zero-load resistance was measured between 1150°C and 1300°C during heating and cooling.

- (1) **Continuous Cooling** – All cooling experiments were carried out under displacement control, where a cooling rate of $0.1 \text{ }^\circ\text{C s}^{-1}$ was used, typical for directional solidification conditions. The load was

continually measured from which the stress (engineering) and the plastic strain was calculated from the measured resistance between 1300°C and 1150°C. Following termination of the test, the sample was cooled under zero-load to room temperature. Since plastic strain accumulates during directional solidification at turbine blade stress concentration features, replicating this experimentally would require notched ETMT specimens. This is not straightforward given the very small cross-section. An alternative approach was therefore adopted to replicate this deformation state in the gauge volume. Here, samples were cooled under displacement control, such that an increased tensile plastic strain, ϵ^{pl} , is produced within sample gauge in addition to the thermal strain, ϵ^{th} . However, it is noted that the tri-axial stress state that develops in turbine blade fillet radii will not be produced. The displacement rates for the different samples is schematically illustrated in Fig. 1. Accordingly, Fig. 1(a) shows the case for samples (U_1 , U_2 , M_1 , and L_1), when a single displacement rate is used, while Fig. 1(b) shows the case for samples (M_2 , M_3 , and L_2) with stepped displacement rates during cooling. Both Figs. 1(a) and (b) refer to as-cast samples. Fig. 1(c) is a schematic representation of near-solutioned samples (S_1 , S_2 , and S_3), when a single displacement rate is used, akin to Fig. 1(a). All samples were of 2×1 mm² cross-section, except for samples U_1 and U_2 , which were 2×2 mm² cross-section.

(2) **Creep Tests** - A rigorous method for conducting “deformation history” dependent creep tests encompassing the stress/strain conditions in the cooling experiments would involve cooling several samples under different displacement rates (\dot{d}) from 1300°C to a series of lower temperatures. A series of flow stress and short-term creep tests at fixed temperatures, stresses would need to be performed and each creep test would constitute a unique sample. The process can be repeated at other discrete temperatures and at a number of lower temperatures. However, such an approach while being exhaustive will require a significant number samples, making it overly time consuming, necessitating some simplification. Two approaches were followed;

- **Method 1 - Use of a single specimen (T₁):** This is schematically illustrated in Fig. 2, starting with tests at 1280°C, followed by tests at successively lower temperatures. At any temperature, the range of applied stresses for the creep tests correspond to that observed in the continuous cooling experiments. The sample was cooled under zero-load between two successive temperatures before the creep experiments were repeated. Using this method, creep tests were carried out at 1280°C, 1260°C and 1240°C, and stresses $\sigma_1 - \sigma_3$, as indicated by the red solid line.
- **Method 2 - Use of multiple specimens (T₂ and T₃):** This is also schematically illustrated in Fig. 2. The sample is cooled under displacement control from 1300°C to a given temperature and a creep test is carried out at the stress that develops on cooling at that temperature. Further creep tests are done at incrementally applied stresses at that temperature. The process is then repeated by cooling from 1300°C to a subsequent lower temperature. Therefore, a single sample is used for creep test at any temperature. Using this approach, creep tests are carried out at 1220°C and corresponding to

stresses σ_{10} , σ_{11} and σ_{12} , as given by the green line and 1180°C corresponding to stresses σ_{13} , σ_{14} and σ_{15} , as indicated by the blue solid line.

- (3) **Flow Stress** – A similar approach to the creep tests was followed, where a single sample was used, i.e. Method 1. However, since plastic strain cumulatively builds up during flow stress testing at lower temperatures, a slight modification was adopted on the principles of Method 2. The temperature range was sub-divided into two regimes, i.e. between 1280°C and 1220°C and between 1190°C and 1170°C. In the first case, flow stress measurements were carried out between 1280°C and 1220°C, where between successive temperatures the samples were cooled under zero-load at 0.1 °C s⁻¹. However, in case of the temperature range between 1190°C and 1170°C, the sample was first cooled under displacement control up to 1190°C, akin to a cooling experiment and subsequent flow stress measurements were carried out at 1190°C, 1180°C and 1170°C. Between successive temperatures the samples were cooled under zero-load at 0.1 °C s⁻¹. Flow stress was measured at a similar strain rate over all temperatures.

2.3 Electron Microscopy

Scanning Electron Microscopy was undertaken in a JEOL 7800F equipped with a Symmetry Electron Backscatter Diffraction (EBSD) camera. Backscattered electron images were collected at 10 kV to show the γ/γ' phases. EBSD maps were collected in a large depth of field mode over typically 1 mm × 0.5 mm areas. In this mode, an extra lens produces a parallel beam of electrons onto the sample resulting in low distortion large area maps. Maps across the surface in the central gauge section of the samples were collected with a step size of 2 μm at a collection speed of 3000 frames per second. Inverse pole figure (IPF) maps were used to identify local changes in grain orientation.

Micro X-ray Fluorescence ($\mu\text{-XRF}$) was used to map the macro-level segregation in the samples. The central gauge portions (approximate dimensions 20 mm × 2 mm of samples U_1 , M_3 , and L_2 were mapped using a Bruker M4 Tornado equipped with two 30 mm² EDS detectors. Maps were collected with a step size of 15 μm at 50 kV and using a current of 580 μA in vacuum. An AlTi 100/25 sandwich filter was used to minimise diffraction peaks. This configuration is best for comparing the composition of key elements of these samples, but the quantification of relatively low energy X-rays (such as those from Al) is compromised (this is not the primary focus of this work). However, the focus is on primarily Re and Cr, which are the key segregating elements to γ phase and Ta that partitions to γ' .

3. Results

3.1 Resistivity and Evolution of Stress and Plastic Strain in near-Solutioned Microstructures

Fig. 3 is an optical micrograph of the cross-section of a near-solutioned test bar. While complete dissolution of the non-equilibrium eutectic phase occurs, the existence of primary dendrite arms indicates that remnant compositional inhomogeneity (micro-segregation) still exists, since in the homogenised condition dendrites are absent. Since the ETMT specimens mainly had cross-sections of $2\text{ mm} \times 1\text{ mm}$ and $2\text{ mm} \times 2\text{ mm}$, the number of primary dendrite arms across a cross-section was determined using superimposed cells of area, $2\text{ mm} \times 1\text{ mm}$, $2\text{ mm} \times 2\text{ mm}$, $3\text{ mm} \times 3\text{ mm}$ and $4\text{ mm} \times 4\text{ mm}$ on Fig. 3. The larger cross-sections approach the typical area of macro-tensile specimens. The number of primary dendrites and associate standard deviation over 15 – 38 representative cell measurements were; $2\text{ mm} \times 1\text{ mm}$: $N = 15 \pm 2$; $2\text{ mm} \times 2\text{ mm}$: $N = 30 \pm 3$; $3\text{ mm} \times 3\text{ mm}$: $N = 70 \pm 4$; $4\text{ mm} \times 4\text{ mm}$: $N = 124 \pm 4$. It is clear that with increasing cross-section, there is minimal variation in number of dendrites across the section, but even for $2\text{ mm} \times 1\text{ mm}$, the variation is at best 15 %.

The composition of the three principal segregating refractory alloying elements, Ta, W and Re was measured using electron microprobe analysis using a $10\text{ }\mu\text{m} \times 10\text{ }\mu\text{m}$ rastered beam in solutioned samples. Approximately 50 measurements were made giving a composition and standard deviation; Ta: $[6.5 \pm 0.4]$ wt. %, W: $[6 \pm 0.5]$ wt. % and Re: $[3 \pm 0.45]$ wt. %. The standard deviation indicates the composition range observed across the microstructure.

Fig. 4(a) plots the resistivity with temperature for the heating/cooling cycles for samples S_1 , S_2 , and S_3 under zero-load. Fig. 4(b) specifically focuses on the temperature interval between 1150°C and 1300°C . Since the intrinsic resistivity of γ and γ' differ with that of γ lower than that of γ' [22], during heating there will be a change in the overall resistance in the gauge volume. Progressive dissolution of γ' commences at $\sim 750^\circ\text{C}$ and terminates at the solvus temperature. The solvus temperature on heating/cooling can be deduced from the onset of the plateau, while the kinetics of dissolution is manifested by the shape of the curves. It can be observed that not only is there a range in solvus temperatures ($\Delta T_{\text{solvus}} = 33\text{ }^\circ\text{C}$) across both heating and cooling curves; see Table 2, but the kinetics of dissolution is also different beyond 1150°C . It is not straightforward to compare the resistivity curves owing to this and to facilitate a comparison it is apt to consider the normalised resistivity, where the resistivity at any temperature is divided by the maximum resistance value; as in Fig. 4(c). This procedure makes comparison between curves possible. A clear gradation in the normalised resistivity curves during both heating and cooling is observed, where at a given temperature the normalised resistivity of sample S_1 is the greatest, while sample S_2 is the lowest.

The implications of resistivity in the evolution of plastic strain and stress during continuous cooling in samples S_1 , S_2 , and S_3 are presented in Figs. 5(a) and (b) respectively. There is a rapid increase in stress over a temperature interval; $\Delta T = 10\text{ }^\circ\text{C}$ between 1300°C and 1290°C ; $\sigma \sim 5.6 - 7.9\text{ MPa}$ beyond which there exists a temperature interval of near-constant stress. This temperature interval for near-constant stress is lowest for S_1 ($\Delta T = 20\text{ }^\circ\text{C}$) and greatest for S_2 ($\Delta T = 50\text{ }^\circ\text{C}$). Below a threshold temperature there is again a rapid increase in stress signifying hardening. This threshold temperature is highest for S_1 ; 1260°C and lowest for S_2 ; 1230°C but

the threshold stress (onset of steep increase) is comparable across all samples; $\sigma \sim 12.2 - 13.1$ MPa; see [Table 2](#). There is also a continuous increase in plastic strain on cooling, with the threshold strain at the onset of hardening in the range; $\varepsilon \sim 0.98 - 1.63$ %. Therefore, the evolution of stress and plastic strain during cooling is dictated by the normalised resistivity. A higher normalised resistivity is associated with a higher threshold temperature for the onset of hardening and accompanied by a greater stress on cooling below the threshold temperature, c.f. lower normalised resistivity.

3.2 Resistivity and evolution of Plastic Strain, Strain Rate and Stress during Cooling in As-Cast Condition

From Eqn. (2) the plot of normalised resistance with temperature follows the pattern of normalised resistivity with temperature, since the temperature dependence of the cross-section, A , and gauge length, L , can be neglected. Hence, the normalised resistance with temperature is considered for the different as-cast samples. The resistance is directly measured using ETMT. In the as-cast condition., $2 \text{ mm} \times 1 \text{ mm}$ and $2 \text{ mm} \times 2 \text{ mm}$ cross-sectional areas were considered, given the variation in the number of dendrites on the cross-section. Fig. 6 plots the normalised resistance for the as-cast samples in the temperature range, 1150°C to 1300°C under zero load conditions. Across the number of samples, the normalised resistance at any temperature is not a unique value, but rather there is a range of values and this variation exists over the entire temperature range. Therefore, the normalised resistances can be viewed to lie in a band whose width is defined by the range in values at a given temperature. Three clusters can be observed within this band and will be classed as sub-bands and are as follows - lowermost sub-band (L_1, L_2), middle sub-band (M_1, M_2, M_3, C_3) and uppermost sub-band ($U_1, U_2, C_1, C_2, C_4, F_1, F_2$). While the $2 \text{ mm} \times 1 \text{ mm}$ specimens lie in all three sub-bands, the $2 \text{ mm} \times 2 \text{ mm}$ samples lie within the uppermost sub-band. Figs. 7(a) and (b) present the evolution of plastic strain and stress during cooling between 1300°C and 1150°C , respectively. As summarised in [Table 3](#), there is an increase in stress with decreasing temperature, but beyond a threshold temperature, this rise is steep. The threshold temperature decreases with decreasing normalised resistance. (L_1, L_2) - 1200°C , (M_1, M_2, M_3) - 1210°C to 1200°C and (U_1, U_2) - 1230°C . The threshold stress lies in a narrow range across the range of normalised resistances; $\sigma \sim 9.6 - 12.6$ MPa. There is also a continuous increase in plastic strain with the value at the onset of hardening being; $\varepsilon \sim 1 - 2.4$ %. A marked exception is sample L_1 , where significant ductility is observed.

Since a range in normalised resistance exists, an analysis of the evolution of plastic strain and stress during cooling requires the following approaches to be adopted; (i) Explore the range of experimental conditions for specimens belonging to a given sub-band or (ii) Consider the implications of a fixed set of experimental conditions on samples across all sub-bands.

Within a given Sub-Band - Samples are considered for a range of imposed grip displacements, with emphasis on the temperature range prior to hardening. Accordingly, grouping in Fig. 6 comprises samples L_1 and L_2 (lowermost sub-band), samples M_1, M_2 and M_3 (middle sub-band) and samples U_1, U_2 (uppermost sub-

band). In the lowermost sub-band, plastic strain is up to three-fold greater for L_1 compared with L_2 . The strain and strain rates for samples in the lowermost sub-band are up to three-fold greater than those in the middle and uppermost sub-bands and with lower stress. In the uppermost sub-band, plastic strain is up to two-fold greater for sample U_2 compared to sample U_1 experiencing a greater stress.

Across Sub-Bands - Samples L_1 , L_2 , M_1 , and U_1 across all sub-bands have been subjected to similar deformation conditions between 1300°C and 1220°C. The largest increase in the plastic strain and strain rate occurs for sample, L_1 , while the greatest increase in stress occurs for sample, U_1 . Therefore, the normalised resistance plays a dominant role in the evolution of plastic strain and stress, like in the case of the near-solutioned condition. Since the normalised resistance (resistivity) is governed by the fraction of γ and γ' phases, the implications of deformation on the as-cast microstructure is next examined.

3.3 Implications of Deformation on the As-cast Microstructure

The as-cast microstructure prior to deformation for a given specimen can be observed on cross-sections at the water-cooled grip ends, where the microstructure is unaffected by the deformation, where Figs. 8(a) and (b) are optical micrographs corresponding to 2 mm × 1 mm and 2 mm × 2 mm, respectively. The number of primary dendrites are near two-fold greater for the higher cross-section; about 29 dendrites for 2 mm × 2 mm and about 12 dendrites for 2 mm × 1 mm, which is consistent with the observations made on the near-solutioned samples. The microstructure within the gauge volume is characterised by the γ' precipitate size/shape as well as crystallography, as in Figs. 9 and 10, respectively. A longitudinal section is considered with the principal direction along the gauge length, while the edge-length is 2 mm. Figs. 9(a) – (c) are back-scattered electron images (BEI) within the gauge length corresponding to samples U_1 , M_3 and L_2 , respectively, while Fig. 9(d) is taken from the water-cooled grip end. Figs. 10(a) and (b) show inverse pole figure (IPF) maps along the gauge length for samples U_1 and M_3 respectively. The γ' precipitates, Figs. 9(a) – (c), show a significant deviation from the near-cube morphology observed at the un-stressed grip ends, Fig. 9(d). The precipitates show distinct elongation, where in case of sample M_3 the morphology approaches a raft-like appearance. There is the marked reduction in the number of the narrow γ channels, unlike in the un-deformed condition. Instead, γ' precipitates are interspersed in the γ matrix and solid-state precipitation of γ' is observed within the γ matrix phase. There also exists a chain of fine equiaxed grains on longitudinal sections along the edges of sample U_1 and extending ~ 25 μm into the section. They are also observed in sample M_3 but extending only ~ 8 μm into the section, as in Figs. 10(a) and (b), respectively. Such edge grains are absent in the case of sample L_2 and therefore no EBSD map is included in Figure 10. Following deformation, there is evidence for markedly elongated γ' precipitates and a chain of fine equiaxed grains along the edges of the sample in the gauge length. However, these grains are absent for samples with prominent ductility. Micro X-ray fluorescence was used to measure the concentration of the segregating elements, Ta, Re and Cr. While Ta segregates to γ' , Re and Cr partition to γ phase. Figs. 11(a) – (c) refer to Re maps corresponding to samples U_1 , M_3 and L_2 , respectively. [Table 4](#)

summarises the average Cr, Ta and Re concentrations measured over representative regions (A-D) indicated in Figs. 11(a) – (c) and also included is the standard deviations across these measurements. The average concentrations of Cr, Ta and Re in all three specimens are similar within the gauge volume.

3.4 Isothermal Flow Stress and Creep Experiments in As-Cast condition

3.4.1 Isothermal Flow Stress

Sample F_1 has a normalised resistance in the uppermost sub-band and the flows stress was measured at 1280°C, 1260°C, 1240°C and 1220°C. This corresponded to the measurements up to/just below the threshold temperature with an average strain rate of $1.2 \times 10^{-5} \text{ s}^{-1}$ over the temperature range. Sample F_2 also has a normalised resistance in the uppermost sub-band and was used for flow stress measurements below the threshold temperature. The sample was cooled under displacement control to 1190°C resulting in a plastic strain of 1.55 %, before flow stress measurements were made. The flow stress was reported at 1190°C, 1180°C and 1170°C with an average strain rate of $1 \times 10^{-5} \text{ s}^{-1}$. Temperature-dependent flow stresses are presented in Fig. 12 and the results are summarised in Table 5. Since a single sample is used, the resultant strain at any temperature is cumulative, i.e. the net plastic strains are; sample F_1 - 1280°C = 0.56 %, 1260°C = 1.08 %, 1240°C = 1.7 %, 1220°C = 2.49 %, sample F_2 - 1190°C = 1.76 %, 1180°C = 1.99 %, 1170°C = 2.34 %. However, in Fig. 12 the plotted plastic strain with stress only refers to the strain induced at that temperature and does not include the prior accumulation from successively higher temperatures. The plastic strains induced at the respective temperatures are therefore; 1280°C = 0.56 %, 1260°C = 0.52 %, 1240°C = 0.62 %, 1220°C = 0.79 %, 1190°C = 0.21 %, 1180°C = 0.23 % and 1170°C = 0.35 % and correspond to the underlined numbers in Table 5.

The temperature-dependent flow stress is compared with the stress that develops during cooling in samples U_1 and U_2 having normalised resistances that lie in the uppermost sub-band in Fig. 6. The average strain rate in the cooling experiments varies as; $\frac{d\varepsilon}{dt} \sim 3 \times 10^{-5} \text{ s}^{-1}$ (U_1) and $5 \times 10^{-5} \text{ s}^{-1}$ (U_2). From Fig. 12, there is negligible hardening up to 1240°C and a near-constant flow stress follows yielding; i.e. $\sigma_{ys} \sim 5 - 8 \text{ MPa}$ between 1280°C and 1240°C. However, at 1220°C hardening occurs, where $\sigma_{ys} \sim 16 \text{ MPa}$ before a saturation stress, $\sigma_{sat} \sim 23 \text{ MPa}$ is reached. Hardening continues to prevail at lower temperatures, where, $\sigma_{ys} \sim 46 \text{ MPa}$ and $\sigma_{sat} \sim 52 \text{ MPa}$ at 1190°C, $\sigma_{ys} \sim 55 \text{ MPa}$ and $\sigma_{sat} \sim 61 \text{ MPa}$ at 1180°C and $\sigma_{ys} \sim 60 \text{ MPa}$ and $\sigma_{sat} \sim 70 \text{ MPa}$ at 1170°C. From Figs. 7(b) and 12, a good correlation is observed between the saturation stress and that developing in sample U_1 up to 1190°C, below which the cooling stress exceeds the saturation stress. In case of sample U_2 , the stress on cooling exceeds the saturation stress from 1240°C, where the difference increases with decreasing temperature and varying from 3 to 10 MPa.

3.4.2 Creep

Creep tests using Method 1 with a single sample were carried out between 1280°C and 1240°C, while multiple samples were used between 1210°C and 1180°C using Method 2. Since negligible hardening is observed up to the threshold stress and the evolution of stress on cooling in this temperature range is comparable across all sample pedigrees (Fig. 7(b) and Table 3), samples C₁ and C₃ having normalised resistances within the uppermost and middle sub-band, were used for creep experiments using Method 1. The maximum stress prior to hardening is, $\sigma = 12.3$ MPa; accordingly, creep tests were carried out in the temperature range; 1300°C to 1240°C for a range of stresses up to a maximum value of 12 MPa. In the cooling experiments for a cooling rate of 0.1 °C s⁻¹, the time duration for a decrease in temperature by 10 °C is 100 s; therefore, creep at any stress was conducted for a maximum time interval of 100 s. This is in sharp contrast to that reported in other studies [23]. Figs. 13(a) and (b) present the evolution of creep strain for samples C₁ and C₃ at three different temperatures; 1280°C, 1260°C and 1240°C, respectively. On the other hand, below the threshold temperature where hardening prevails, samples C₂ and C₄ with normalised resistances in the uppermost sub-band were used. The evolution of creep strain for samples C₂ and C₄ at; 1220°C, 1180°C is presented in Figs.13(c) and (d), respectively. Like in the flow stress; Fig. 12, the creep strain in Figs. 13(a) – (d) corresponds to strain induced at that temperature and not the cumulative value. Accordingly, in Table 6, the strain induced is underlined, as in Table 5 for flow stress. The net plastic strain at any temperature however is a sum of that arising from prior creep experiments at the same and/or higher temperatures. In case of C₂, the sample was cooled under displacement control to 1220°C, while in case of C₄, cooling was under displacement control to 1180°C and the corresponding plastic strains were 1.55 % and 2.32 % respectively prior to creep tests. It can be observed that primary creep is negligible and steady-state creep dominates and therefore it is justifiable to represent the steady-state creep rate by an Arrhenius equation.

$$\dot{\varepsilon}^{cr} = A_0^{cr} \exp\left(-\frac{Q^{cr}}{RT}\right) \left(\frac{\sigma}{\sigma_0}\right)^{n^{cr}} = \frac{1}{\tau} (\sigma)^n \exp\left(\frac{-Q}{RT}\right) \quad (3)$$

where, τ is the viscosity parameter (s), Q is the activation energy and n the stress exponent, where the superscript “cr” has been dropped. Accordingly, Fig. 14 is a plot of $\ln\left(\frac{d\varepsilon}{dt}\right)$ versus $\ln \sigma$. Secondary (steady-state) creep prevails even for such small-time intervals. While, $n \sim 4.3 - 4.9$ in the temperature range, 1280°C to 1240°C, $n \sim 6.8 - 7.6$ in the temperature range, 1220°C to 1180°C. It was therefore inappropriate to use a unique value for the stress exponent (n) in deducing a constitutive law across the entire temperature range. Accordingly, only the temperature range, 1280°C to 1240°C is considered where hardening is absent. Using best-fit least squares method; $n = 4.3$, $\tau = 9.6 \times 10^{-13}$ s and $Q = 598$ kJ mol⁻¹.

4. Discussion

One possible reason for the range in solvus temperature could arise from variation in composition across the different ETMT specimen gauge volumes from macro-segregation. However, this explanation can be discarded, since the concentration of the principal solute species segregating to γ and γ' phases is similar within the gauge

regions for specimens spanning the three sub-bands of normalised resistance, as summarised in [Table 4](#). A second possible reason is the existence of micro-segregation. In the as-cast condition, concentration gradients develop within the solid owing to limited solid-state diffusion in the dendrites in presence of refractory elements like Ta, W and Re with sluggish diffusion kinetics [[10](#), [29](#)]. This can be illustrated using the binary phase diagram in [Fig. 15](#). The local solidification path has been schematically illustrated for two dendrite cross-sections, where the red and blue curves correspond to the average solid composition. The S/L interfacial compositions however follow the solidus and liquidus lines respectively. In this representative case solidification terminates within the single phase-field, but the arguments are equally valid when a eutectic reaction occurs. Solidification for the two freezing paths terminates at T_1 and T_2 for the red and blue curves respectively, where in the latter case, a larger freezing range is present. At temperature, T , there is a range in solid composition; $C_\gamma \leq C < C_2$, where γ' precipitates exist when the solidification path corresponds to the blue line, while in case of the red line, for all compositions $C < C_\gamma$, only γ phase exists. Therefore, the range in solvus temperature can be attributed to the local freezing path., which is accentuated in case of miniature specimens, when the number of dendrites are few; typically, 15 in $2 \text{ mm} \times 1 \text{ mm}$ cross-sections. When the number of dendrites increase, as in macro-specimens this range in solvus temperature becomes increasingly less pronounced.

The onset of hardening commences beyond a critical threshold fraction of γ' precipitates within the γ matrix for as-cast or solutioned samples. Unfortunately, a calculation of the precipitate fraction could not be performed as the γ and γ' phases' resistivities as a function of temperature is not known. Nevertheless, for a reported thermodynamic and kinetic simulation [[29](#)], a minimum mole-fraction of about 0.2 (dendrite core) and a maximum of about 0.4 (periphery of dendrite lobe) was reported across the dendrite cross-section in the as-cast condition at 1227°C . This approximates a range of γ' fraction when hardening will begin to dominate. In the as-cast condition, however, there also exists γ' within the inter-dendritic region, which constitutes the non-equilibrium phase, but absent in the near-solutioned condition. Moreover, this eutectic morphology will exist above the solvus, i.e. at 1300°C since it is formed in the liquid state and in CMSX-4 this is approximately 10 % [[29](#)]. Despite the existence of eutectic γ' with an associated higher local solvus temperature compared with the near-solutioned condition (absence of eutectic), the onset of precipitation hardening in the as-cast conditions occurs at a lower temperature compared with the near-solutioned condition ([Tables 2 and 3](#)). It can be inferred that eutectic γ' does not contribute to precipitation hardening and plays no role, unlike solid-state precipitated γ' within the dendrites. This is a key inference. Furthermore, owing to larger solid composition range in the as-cast condition compared to the solutioned state, the kinetics for the evolution of γ' during cooling is lower than in the near-solutioned case, i.e. $\frac{df_{\gamma'}}{df_s}_{\text{near-solutioned}} > \frac{df_{\gamma'}}{df_s}_{\text{as-cast}}$, where f_s = solid-fraction, corresponding to C_s . Consequently, the critical fraction γ' required for precipitation hardening will develop over a larger temperature range in the as-cast condition compared with the solutioned state.

Within regions of compositional inhomogeneity and differing solvus temperature, the deformation must also affect γ' morphology. Stress also affects the evolution of γ' shape, as observed in rafting, which are oriented perpendicular to the applied stress when lattice misfit is negative ($a_{\gamma'} < a_{\gamma}$) [30, 31]. In Figs. 9(a) – (c) the γ' morphology is elongated but not completely rafted and suggests a role of the macroscopic stress state on misfit. The two main considerations during continuous cooling that cause morphological changes are; (a) limited time dictated by the local cooling rate, which must have implications to stress driven coarsening and (b) the γ' precipitates nucleate within the strained matrix phase below the solvus. Detailed microstructure analysis using transmission electron microscopy is needed to identify the dislocation sub-structure that forms during deformation, as reported elsewhere [14, 32]. Nevertheless, other microscopic clues are present that relates the superalloy solid to deformation processes, as in Figs. 10(a) – (c). Since the samples in the cooling experiments are cooled under zero-load from 1150°C to room temperature on termination of the test, the equiaxed grains in samples \mathbb{U}_1 and \mathbb{M}_3 must have originated above 1150°C. Plastic deformation of secondary dendrite arms at edges resulting in equiaxed grains occurs when the stress exceeds the yield stress. This is most pronounced for least ductile sample \mathbb{U}_1 , where the stresses are significantly greater compared with \mathbb{M}_3 and \mathbb{L}_2 . Further, such pre-existing equiaxed grains can be potent nuclei for re-crystallisation during subsequent heat treatment, as was reported in [13].

It is interesting to compare the flow stress with the results observed from the cooling experiments. Above the threshold temperature, not only is the stress comparable across the range of normalised resistances, but also agrees well with the flow stress. In case of samples \mathbb{U}_1 and \mathbb{U}_2 between 1280°C and 1240°C the stress agrees closely with the saturation stresses in Fig. 12, indicating the role of visco-plastic deformation or creep with limited precipitation hardening. With further cooling, there is increasing difference in stress between sample \mathbb{U}_2 , Fig. 7(b) and the saturation stress at a given temperature, Fig. 12, unlike in case of \mathbb{U}_1 . There are two reasons to account for this.

- First, the difference in strain rates corresponding to the flow stress and cooling experiments was $\Delta\dot{\epsilon} \sim 2 \times 10^{-5} \text{ s}^{-1}$ for \mathbb{U}_1 , while it is $\Delta\dot{\epsilon} \sim 4 \times 10^{-5} \text{ s}^{-1}$ for \mathbb{U}_2 . At temperatures close to the γ' solvus, when creep is dominant, the strain rate is important. The higher strain rate in \mathbb{U}_2 therefore accounts for the greater stress, from reduced visco-plasticity.
- Second, history dependence constitutes the second reason. In case of \mathbb{U}_1 , the plastic strain at any temperature during cooling between 1190°C and 1170°C, is at most 0.7 % larger than the flow stress measurements. However, in \mathbb{U}_2 , the plastic strain is at least 2% greater than in the flow stress experiments.

Therefore, accumulated deformation at successively higher temperature as well as the strain rate plays a pivotal role in the evolution of stress and strain during cooling.

Creep is an important aspect in these experiments. This is best observed when comparing;

- (i) Samples across sub-bands under constant deformation conditions, or
- (ii) Across samples in a given sub-band under varying deformation rates.

In (i), i.e. when comparing samples L_1 , M_1 , L_2 and U_1 , the most noticeable observation is the extreme ductility exhibited by sample L_1 in the lowermost sub-band, while in (ii) when comparing samples U_1 and U_2 , it is the larger plastic strain observed in case of U_2 compared with U_1 . The need for two creep testing methods arises from this history-dependence. Specifically, at lower temperatures, where precipitation hardening dominates it is pertinent to use multiple samples, rather than a single sample. In addition, strain rate is critical as observed in the flow stress measurements. In case of multiple samples, while the overall strain rate is typically $0.5 - 5 \times 10^{-5} \text{ s}^{-1}$, in case of a single sample the range in strain rate is lower and typically $1.5 - 2.5 \times 10^{-5} \text{ s}^{-1}$, although few higher values also exist (Table 6). Since multiple creep tests are done on a single sample, it is important to ascertain the net plastic strain after creep tests. The total plastic strain in creep samples C_1 and C_3 at 1280°C, 1260°C and 1240°C exceed that for both U_1 and U_2 , while the difference between sample U_1 and creep samples C_2 and C_4 at 1220°C and 1180°C is smaller (Table 6). Notwithstanding this difference in plastic strain, the role of history-dependent deformation is captured.

The Norton equation has been used for the creep strain rate since steady-state creep rate occurs within the approximately 100 s test duration. The stress exponent, $n \sim 4.3 - 4.9$ is consistent with dislocation models developed for octahedral glide-controlled creep, where $n \sim 6$ has been reported for CMSX-4 at 1288°C, where precipitation hardening can be neglected [33]. However, $n \sim 6.8 - 7.6$ below the threshold temperature, where precipitation hardening occurs is comparable to $n \sim 7$ reported in [14] at 1100°C. The difference in exponent below 1220°C, clearly indicates the implications of precipitation hardening. By considering the temperature range, 1280°C to 1240°C, where deformation is within γ phase, $n \sim 4.3$ and the calculated activation energy, $Q \sim 598 \text{ kJ mol}^{-1}$ shows reasonable agreement with $Q \sim 500 \text{ kJ mol}^{-1}$ in [34] and $Q \sim 469 \text{ kJ mol}^{-1}$ in [35]. However, these activation energies correspond to the temperature range 800°C to 950°C, while a value of 773 kJ mol^{-1} at 1100°C has been reported in [14]. These parameters are the same for both samples C_1 and C_3 over the temperature range before precipitation hardening occurs, in spite of recording different normalised resistances. This is not surprising, since the evolution of stress and plastic strain across the middle and uppermost sub-band begins to deviate significantly only below the critical temperature when hardening begins to dominate.

There are some key implications of this study. First, it is now possible to use a constitutive equation for creep that captures the history dependence of deformation to model the evolution of plastic strain and stress on cooling from temperatures close to solvus. Second, unlike previous studies, the approach of using a single equation can only be used over a small temperature range before precipitation hardening begins to dominate. Third, location specific aspects arise, especially in regions where the number of dendrites across the cross-section is small. This specifically relates to fillet radii in the aerofoil of turbine blades, where conditions akin to that existing in miniature testing are encountered.

Conclusions

- (1) Location specific properties become increasingly dominant in thermo-mechanical deformation for cross-sectional area $\leq 2 \text{ mm}^2$ approaching solvus temperature. This is prevalent in the as-cast condition, where the normalised resistance/resistivity can be used to classify micro-segregation.
- (2) On cooling from 1300°C to 1150°C;
 - (a) Creep within γ phase accompanied by a small increase in stress occurs initially up to a critical temperature, below which a rapid increase in stress occurs from precipitation hardening of γ' .
 - (b) With decreasing normalised resistance, the temperature for the onset of hardening decreases accompanied with a lower stress compared with higher normalised resistance.
- (3) Short-term creep experiments to capture the history-dependent deformation have been designed in the temperature range 1300°C to 1220°C and between 1220°C to 1180°C, when precipitation hardening prevails.
 - (a) Steady-state (secondary) creep was shown to follow an Arrhenius-type equation. Between 1300°C to 1220°C, the best-fit parameters are; n (stress exponent) ~ 4.3 and Q (activation energy) $\sim 598 \text{ kJ mol}^{-1}$, which is consistent with dislocation glide creep in γ phase.
 - (b) A constitutive equation is therefore proposed between 1300°C to 1240°C to calculate the evolution of stress and plastic strain during cooling in this temperature range.

Acknowledgments

C.P. would like to acknowledge the grant from Innovation Fellowship funded by Engineering and Physical Science Research Council (EPSRC), UK Research and Innovation (grant number: EP/S000828/1).

Data availability

The raw/processed data required to reproduce these findings cannot be shared at this time as the data also forms part of an ongoing study.

Declaration of competing interest

The authors declare that they have no known competing financial interests or personal relationships that could have appeared to influence the work reported in this paper.

References

- [1] D. C. Cox, B. Roebuck, C. M. F. Rae, R. C. Reed, Recrystallisation of single crystal superalloy CMSX-4, *Mater. Sci. Technol.*, 19 (2003) 440 – 446.

- [2] M. Dupeux, J. Henriot, M. Ignat, Tensile stress relaxation behaviour of Ni-based superalloy single crystals between 973 and 1273K, *Acta Metall.*, 35 (1987) 2203 – 2212.
- [3] H. Wang, B. Clausen, C. N. Tome, P. D. Wu, Studying the effect of stress relaxation and creep on lattice strain evolution of stainless steel under tension, *Acta Mater.*, 61 (2013) 1179 – 1188.
- [4] J. Svoboda, P. Lukas, Modelling of recovery controlled creep in nickel-base superalloy single crystals, *Acta Mater.*, 45 (1997) 125 – 135.
- [5] J. Preußner, Y. Rudnik, H. Brehm, R. Volkl, U. Glatzel, A dislocation density based material model to simulate the anisotropic creep behavior of single-phase and two-phase single crystals, *Int. J. Plast.*, 25 (2009) 973 – 994.
- [6] J. Cormier, G. Cailletaud, Constitutive modeling of the creep behavior of single crystal superalloys under non-isothermal conditions inducing phase transformations, *Mater. Sci. Eng. A*, 527 (2102) 6300 – 6312.
- [7] J. Cormier, M. Jouiad, F. Hamon, P. Villechaise, X. Milhet, Very high temperature creep behavior of a single crystal Ni-based superalloy under complex thermal cycling conditions, *Philos. Mag. Lett.*, 90 (2010) 611 – 620.
- [8] J. Cormier, X. Milhet, J. Mendez, Non-isothermal creep at very high temperature of the nickel-based single crystal superalloy MC2, *Acta Mater.*, 55 (2007) 6250 – 6259.
- [9] J-B. le Graverend, J. Cormier, F. Gallerneau, P. Villechaise, S. Kruch, J. Mendez, A microstructure-sensitive constitutive modeling of the inelastic behavior of single crystal nickel-based superalloys at very high temperature, *Int. J. Plast.*, 59 (2014) 55 – 83.
- [10] C. E. Campbell, W. J. Boettinger, U. R. Kattner, *Acta Mater.*, 50 (2002) 775 – 792.
- [11] N. Warnken, D. Ma, A. Drevermann, R. C. Reed, S. G. Fries, I. Steinbach, Phase-field modelling of as-cast microstructure evolution in Ni-based superalloys, *Acta Mater.*, 57 (2019) 5862– 5875.
- [12] L. Wang, F. Pyczak, J. Zhang, L. H. Lou, R. F. Singer, *Mater. Sci. Eng. A*, 532 (2012) 487 – 492.
- [13] H. N. Mathur, C. Panwisawas, C. N. Jones, R. C. Reed, C. M. F. Rae, Nucleation of recrystallisation in castings of single crystal Ni-based superalloys, *Acta. Mater.*, 129 (2017) 112 – 123.
- [14] C. Panwisawas, H. Mathur, J-C. Gebelin, D. Putman, C. M. F. Rae, R. C. Reed, Prediction of recrystallization in investment cast single-crystal superalloys, *Acta Mater.*, 61 (2013) 51 – 66.
- [15] N. D'Souza, J. Kelleher, S. Kabra, C. Panwisawas, Visco-plasticity during in-situ cooling from solidification of a Ni-base single crystal superalloy using neutron diffraction. *Mater. Sci. Eng. A*, 681 (2017) 32 – 40.
- [16] D. M. Collins, N. D'Souza, C. Panwisawas, In-situ neutron diffraction during stress relaxation of a single crystal Ni-base superalloy, *Scr. Mater.*, 131 (2017) 103 – 17.

- [17] J. Coakley, R. C. Reed, J. L. W. Warwick, K. M. Rahman, D. Dye, Lattice strain evolution during creep in single crystal superalloys, *Acta Mater.*, 60 (2012) 2729 - 2738.
- [18] E. Wu, G. Sun, B. Chen, J. Zhang, V. Ji, V. Klosek, M-H Mathon, Neutron diffraction study of strain/stress states and subgrain defects in a creep deformed single crystal superalloy, *Metall. Mater. Trans. A*, 45 (2014) 139 – 146.
- [19] L. Zhonglin, Z. Dandan, S. Xianglin, X. Qingyan, L. Baicheng, Role of as-cast dendritic microstructure in recrystallization of a Ni-based single crystal superalloy, *J. Alloy. Comp.*, 660 (2016) 115 – 124.
- [20] L. Zhonglin, X. Qingyan, L. Baicheng, Microstructure simulation on recrystallization of an as-cast nickel based single crystal superalloy, *Comp. Mater. Sci.*, 107 (2015) 122 – 133.
- [21] B. Roebuck, D. C. Cox, R. C. Reed, An innovative device for the mechanical testing of miniature specimens of superalloys, *Superalloys 2004*, TMS, Warrendale, PA, (2004) 523 – 528.
- [22] B. Roebuck, D. C. Cox, R. C. Reed, The temperature dependence of gamma prime volume fraction in a Ni-base single crystal superalloy from resistivity measurements, *Scr. Mater.*, 44 (2001) 917 – 921.
- [23] G. Sutton, A. Greenhen, B. Roebuck, G. Machin, Imaging phosphor thermometry from T = 20 °C to 450 °C using the time-domain intensity ratio technique, *First Int. Conf. on Phosphor Thermometry*, Glasgow, UK, July 25-27, 2018 and *Measurement Science and Technology*, 30(4) (2019) 044002(11pp).
- [24] S. Sulzer, E. Alabort A. Nemeth, B. Roebuck, R. C. Reed, On the rapid assessment of mechanical behaviour of a prototype Ni-based superalloy using small-scale testing, *EuroSuperalloys 2018*, *Metall. Mater. Trans. A*, 49 (2018) 214 – 4235.
- [25] B. Roebuck, M. Brooks and A. Pearce, *Good Practice Guide for Miniature ETMT Tests*, NPL Good Practice Guide No. 137, January 2016.
- [26] L. Zhonglin, X. Jichun, X. Qingyan, L. Jiarong, L. Baicheng, Deformation and re-crystallisation of single crystal Ni-based superalloys during investment casting, *J. Mater. Process. Technol.*, 217 (2015) 1 – 12.
- [27] C. Panwisawas, J-C. Gebelin, R. C. Reed, Analysis of the mechanical deformation arising from investment casting of directionally solidified Ni-based superalloys, *Mater. Sci. Technol.*, 29 (2013) 843 – 853.
- [28] C. Panwisawas, N. D’Souza, D. M. Collins, A. Bhowmik, B. Roebuck, History dependence of the microstructure on time-dependent deformation during in-situ cooling of a Ni-based single crystal superalloy, *Metall. Mater. Trans. A*, 49 (2018) 3963 – 3972.
- [29] C. Walter, B. Hallstedt, N. Warnken, Simulation of Solidification of CMSX-4, *Mater. Sci. Eng. A*, 397 (2005) 385 – 390.
- [30] T. Ohashi, K. Hidaka, S. Imano, Elastic stress in single crystal Ni-base superalloys and the driving force for their microstructural evolution under high temperature creep conditions. *Acta Mater.*, 45 (1997) 1801 - 1810.

- [31] A. Ma, D. Dye, R. C. Reed, A model for the creep deformation behaviour of single crystal superalloy CMSX-4, *Acta Mater.*, 56 (2008) 1657 – 1670.
- [32] C. Panwisawas, N. D'Souza, D. M. Collins, A. Bhowmik, The contrasting roles of creep and stress relaxation in the time-dependent deformation during in-situ cooling of a Ni-based single crystal alloy, *Sci. Rep.*, 7 (2017) 11145.
- [33] A. Ephishin, B. Fedelich, G. Nolze, S. Schriever, T. Feldmann, M. Ijaz, B. Viguier, D. Poquillon, Y. Le Bouar, A. Ruffini, A. Finel, Creep of single crystals of Ni-based superalloys at ultra-high homologous temperature, *Metall. Mater. Trans. A*, 49 (2018) 3973 – 3987.
- [34] W. Schneider, H. Mughrabi, in B. Wilshire, R. W. Evans (eds.) *Creep and Fracture of Engineering Materials and Structures*, The Inst. of Mater. London, 1993, p. 209.
- [35] J. Svoboda, P. Lukas, Activation energy of creep in $\langle 001 \rangle$ oriented superalloy CMSX-4 single crystals, *Mater. Sci. Eng. A*, 234 – 236 (1997) 173 – 176.

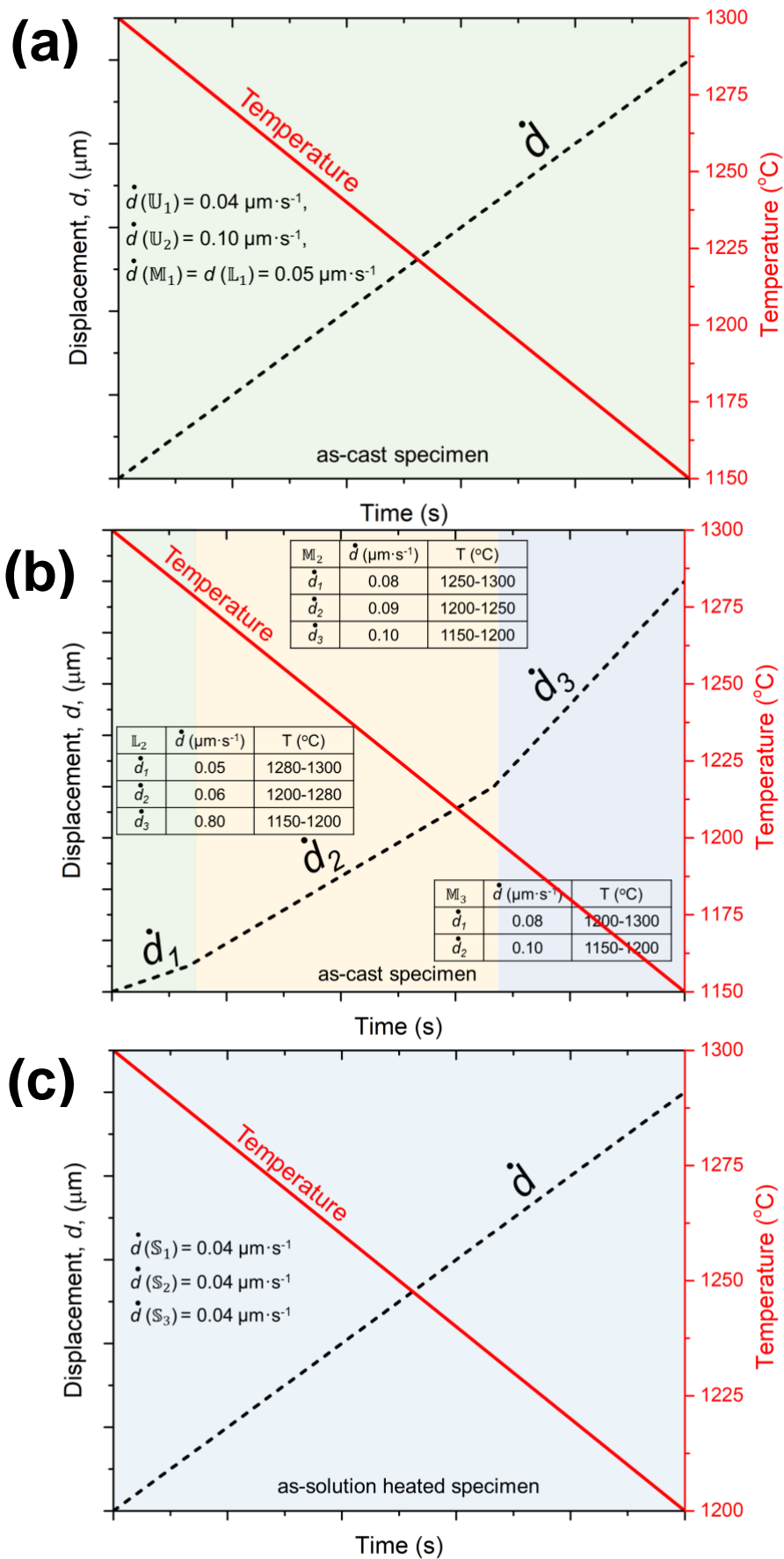


Fig. 1: Schematic illustrations of loading conditions for; (a) as-cast specimens with single displacement rate (samples U_1 , U_2 , M_1 , and L_1), (b) as-cast specimens with multiple displacement rates (samples M_2 , M_3 , and L_2), and (c) as-solutioned (heated treated) specimens with single displacement rate (samples S_1 , S_2 , and S_3).

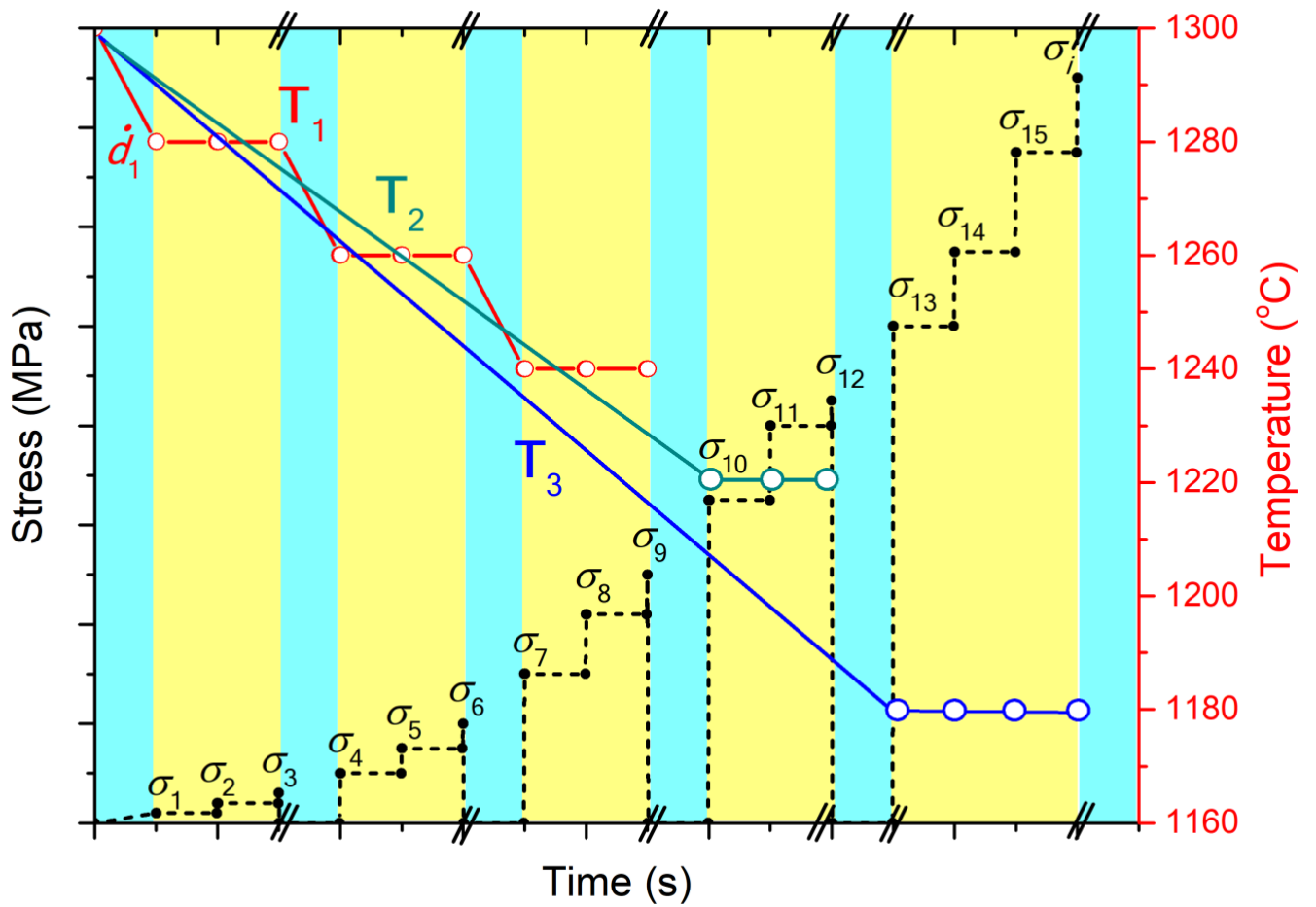


Fig. 2: Schematic showing the different approaches for conducting creep tests to capture the history dependence of prior accumulated deformation using two methods.

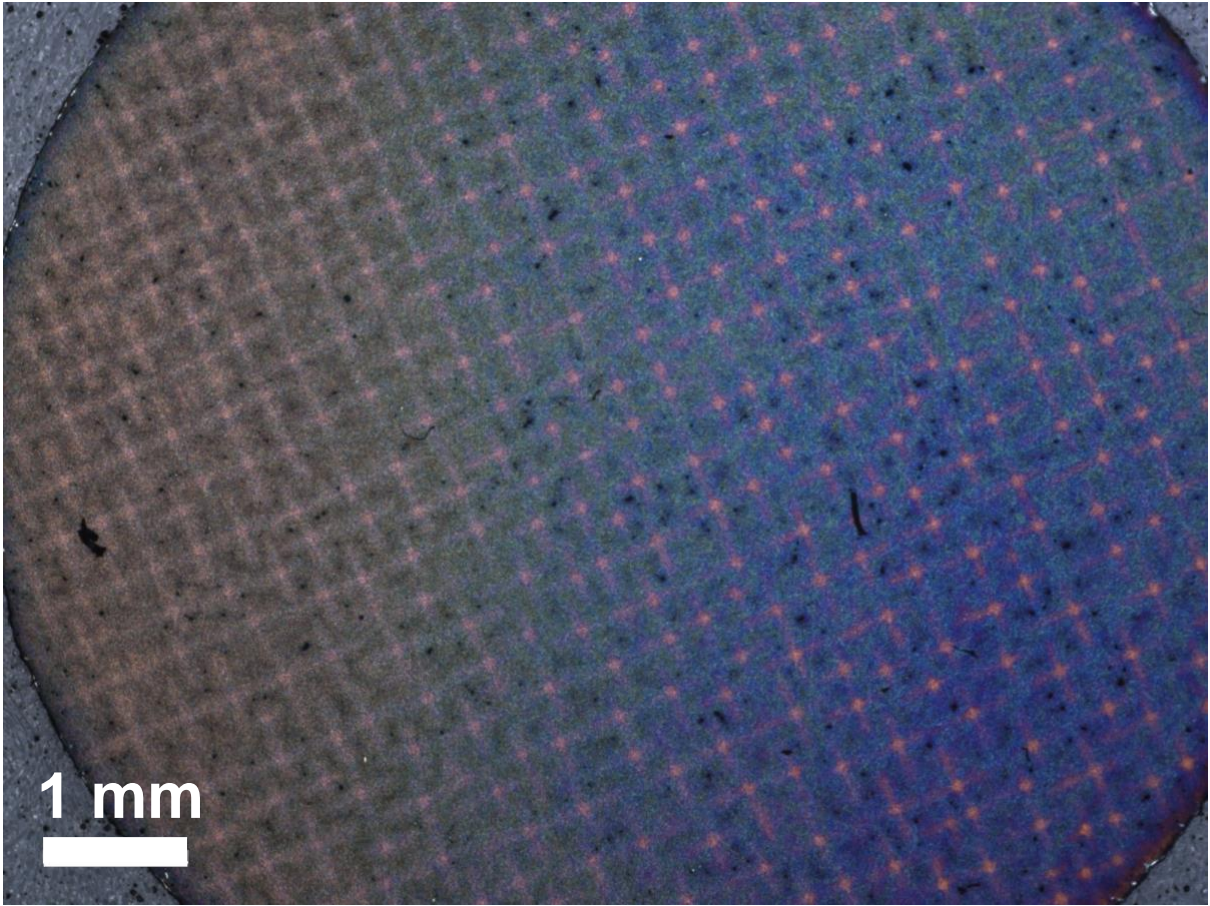


Fig. 3: Optical micrograph of the transverse cross-section of a near-solutioned test bar.

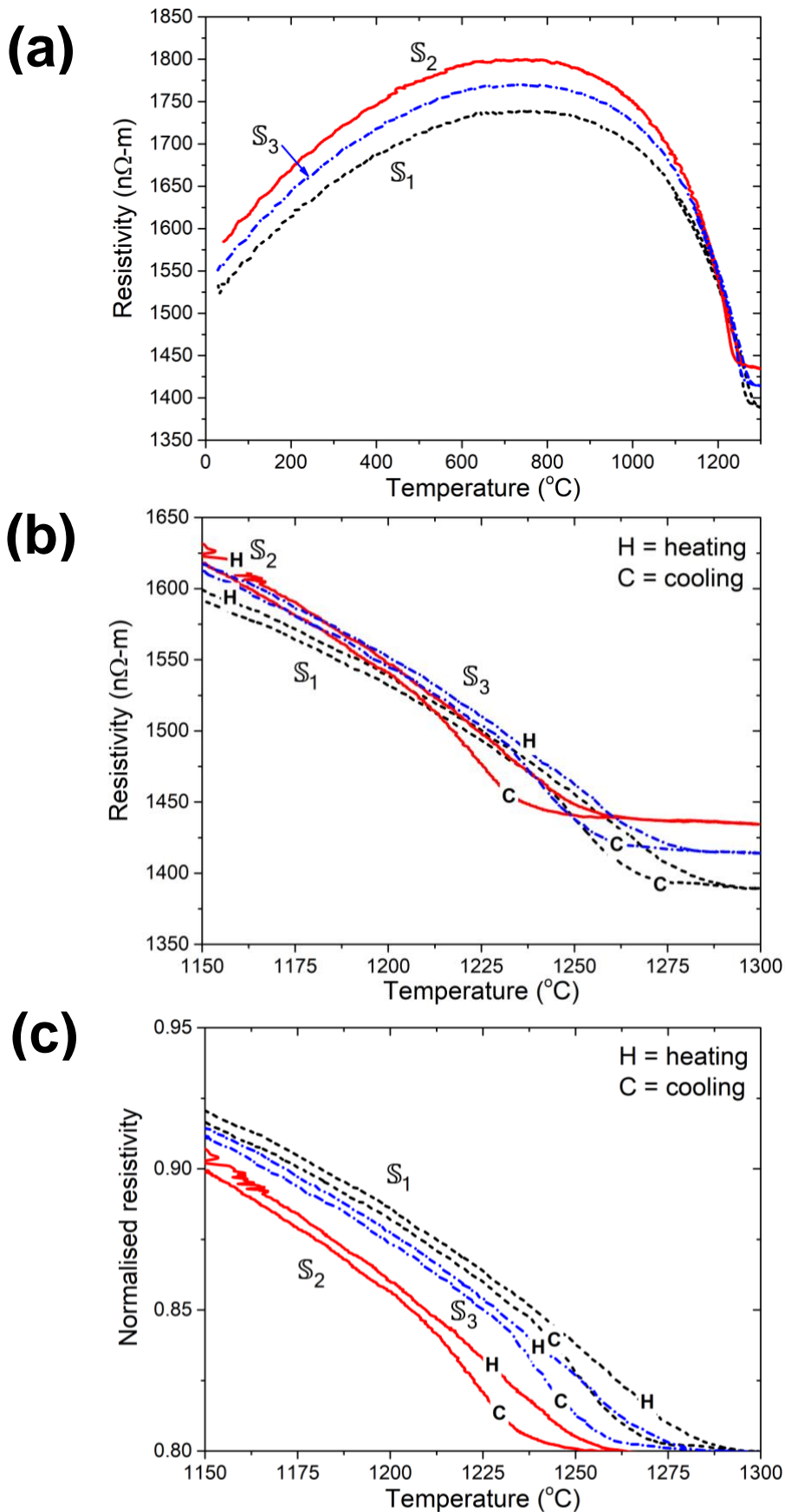


Fig. 4: Variation of resistivity with temperature of near-solutioned test bar specimens, S_1 , S_2 and S_3 during heating and cooling cycles under zero-load; (a) Resistivity between $1300^{\circ}C$ and room temperature (RT), (b) Resistivity between $1300^{\circ}C$ and $1150^{\circ}C$, (c) Normalised resistivity between $1300^{\circ}C$ and $1150^{\circ}C$.

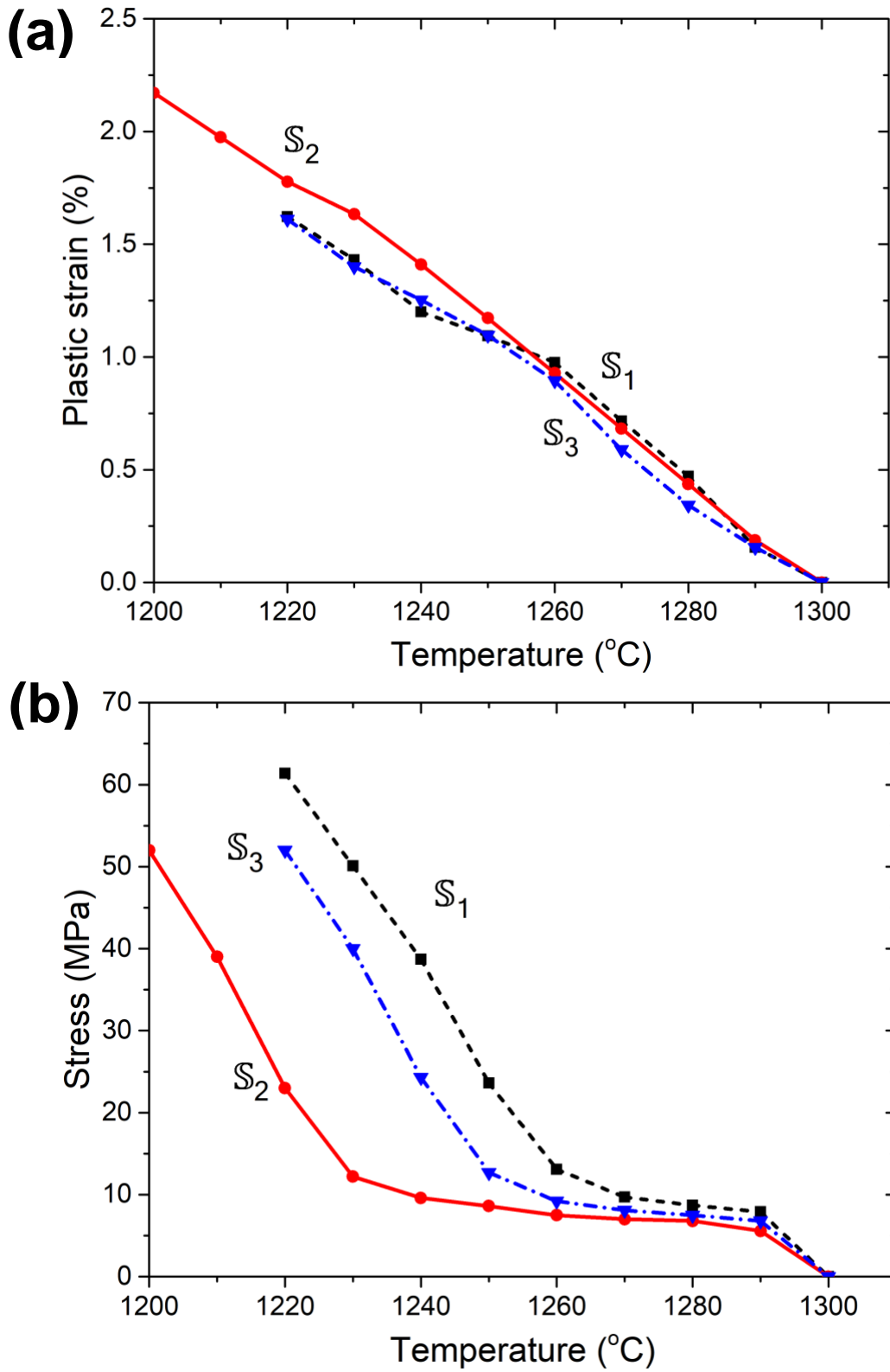


Fig. 5: Evolution of plastic strain and stress of near-solutioned test bar specimens, S_1 , S_2 and S_3 during continuous cooling under displacement control between 1300°C and 1200°C; refer Table 3; (a) Plastic strain, (b) Stress.

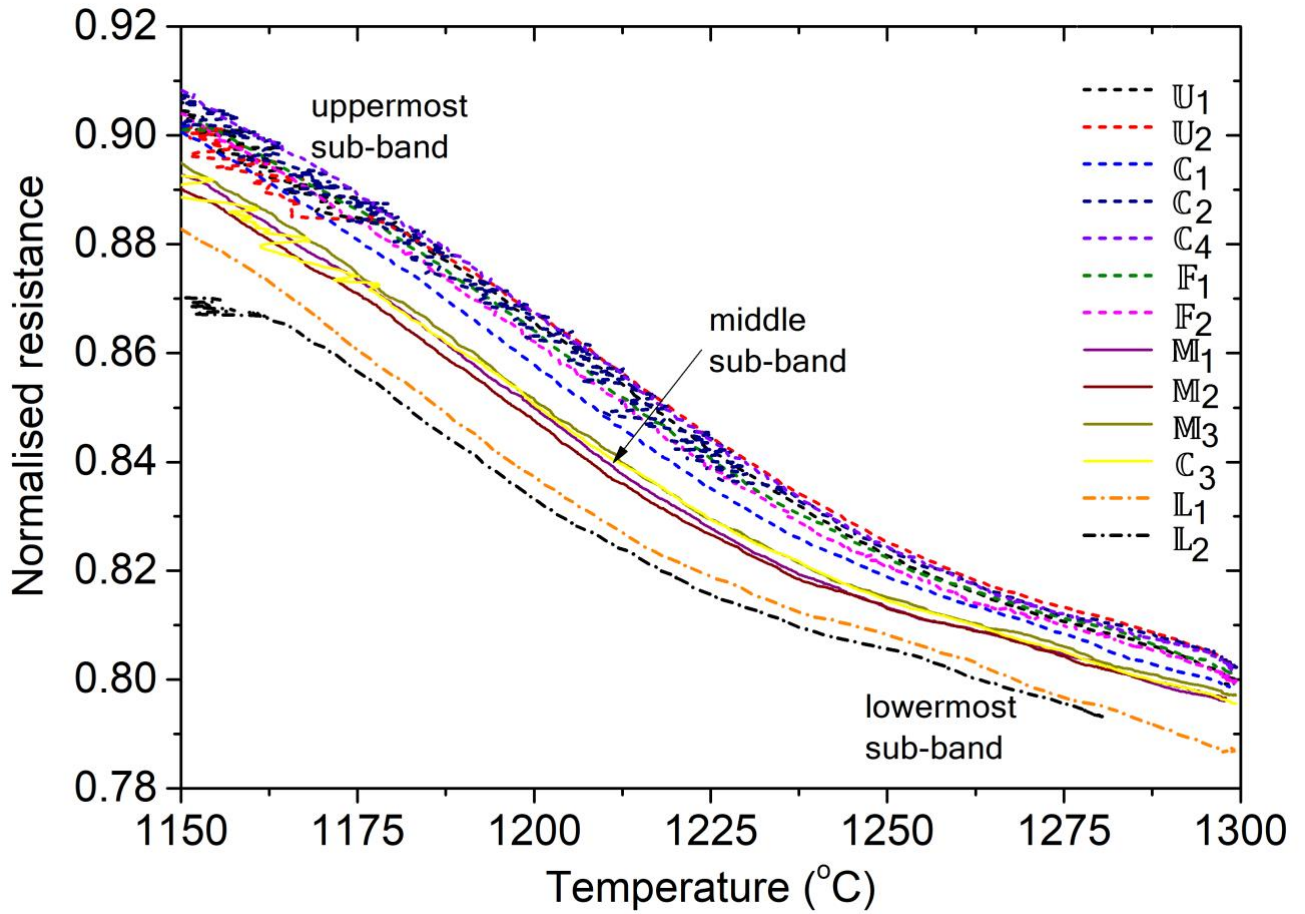


Fig. 6: Variation of normalised resistance with temperature of as-cast samples during heating and cooling cycles under zero-load between 1300°C and 1150°C.

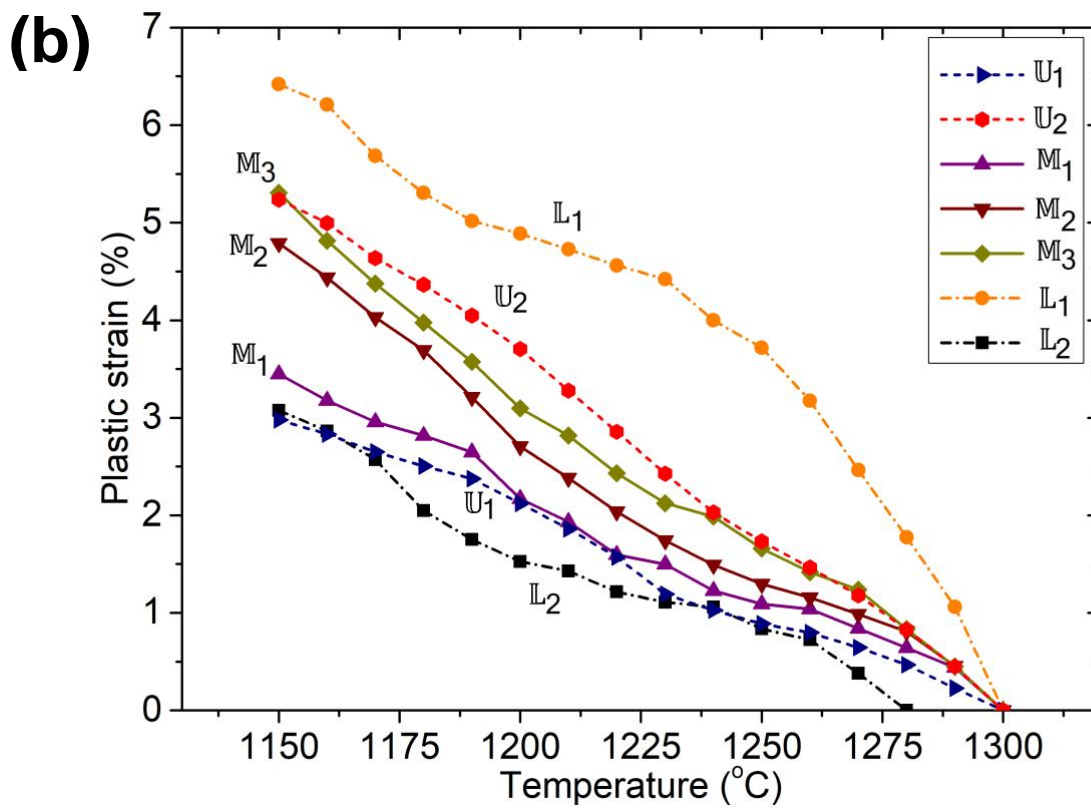
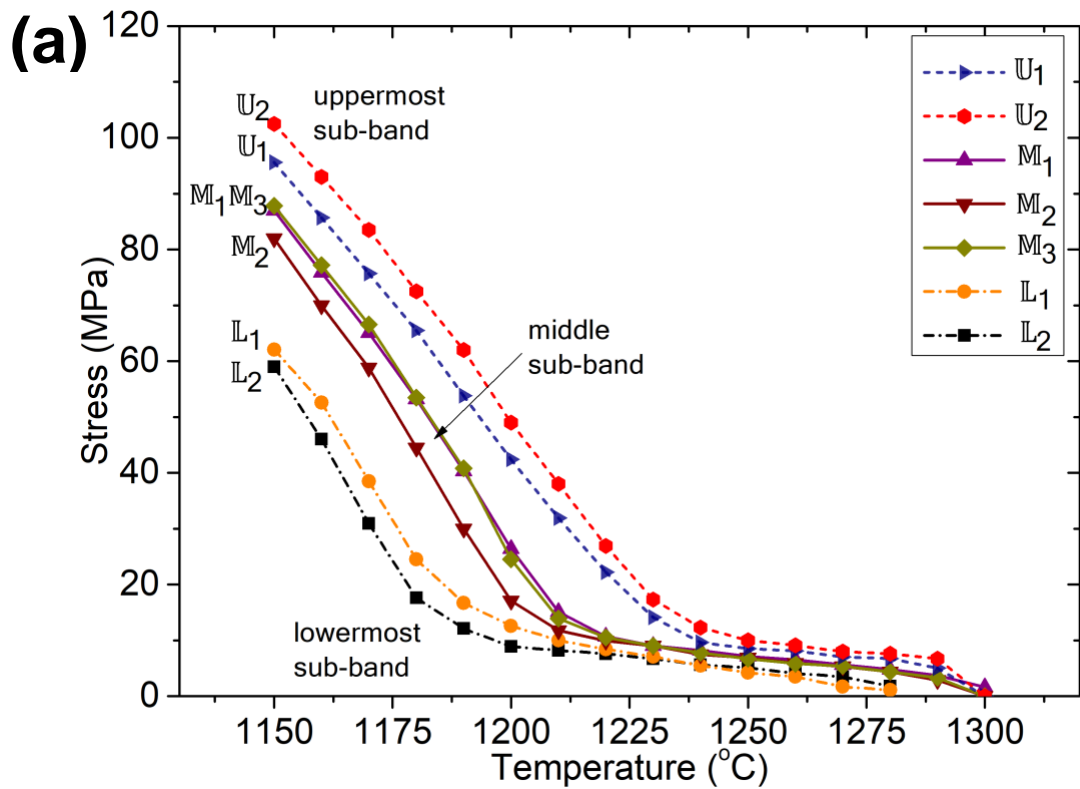


Fig. 7: Evolution of plastic strain and stress of as-cast samples during continuous cooling under displacement control between 1300°C and 1150°C ; refer Table 3; (a) Plastic strain, (b) Stress.

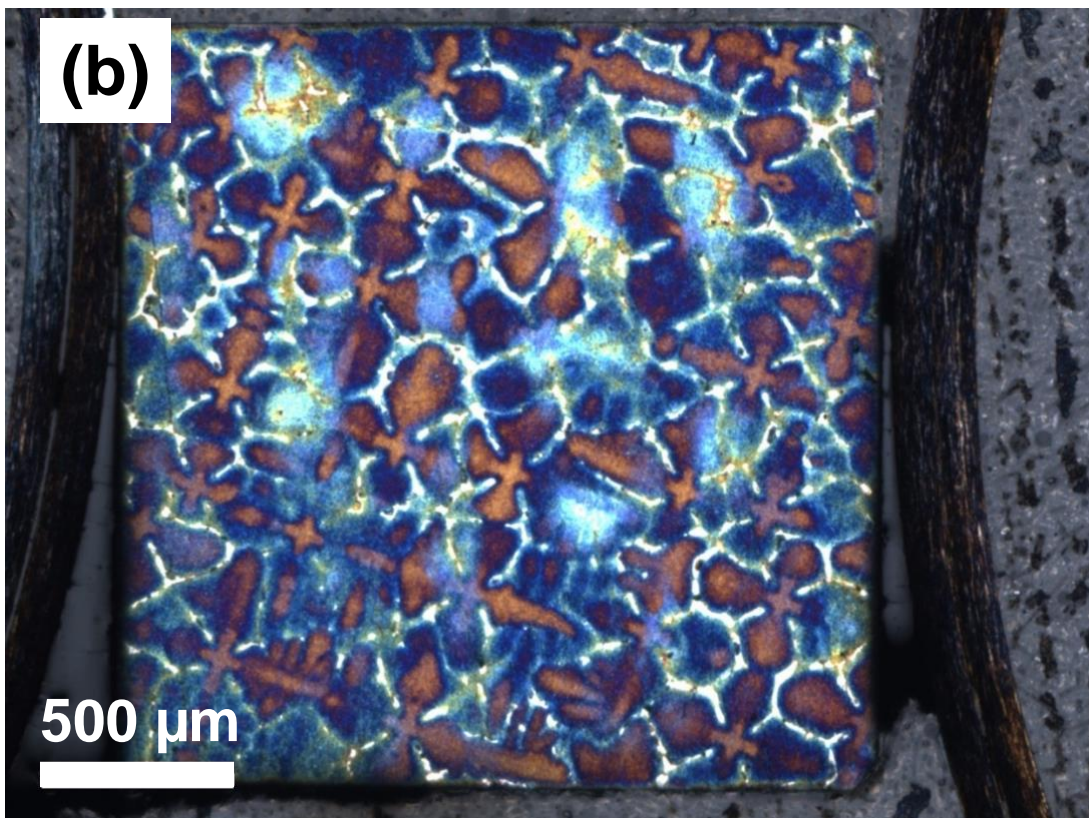
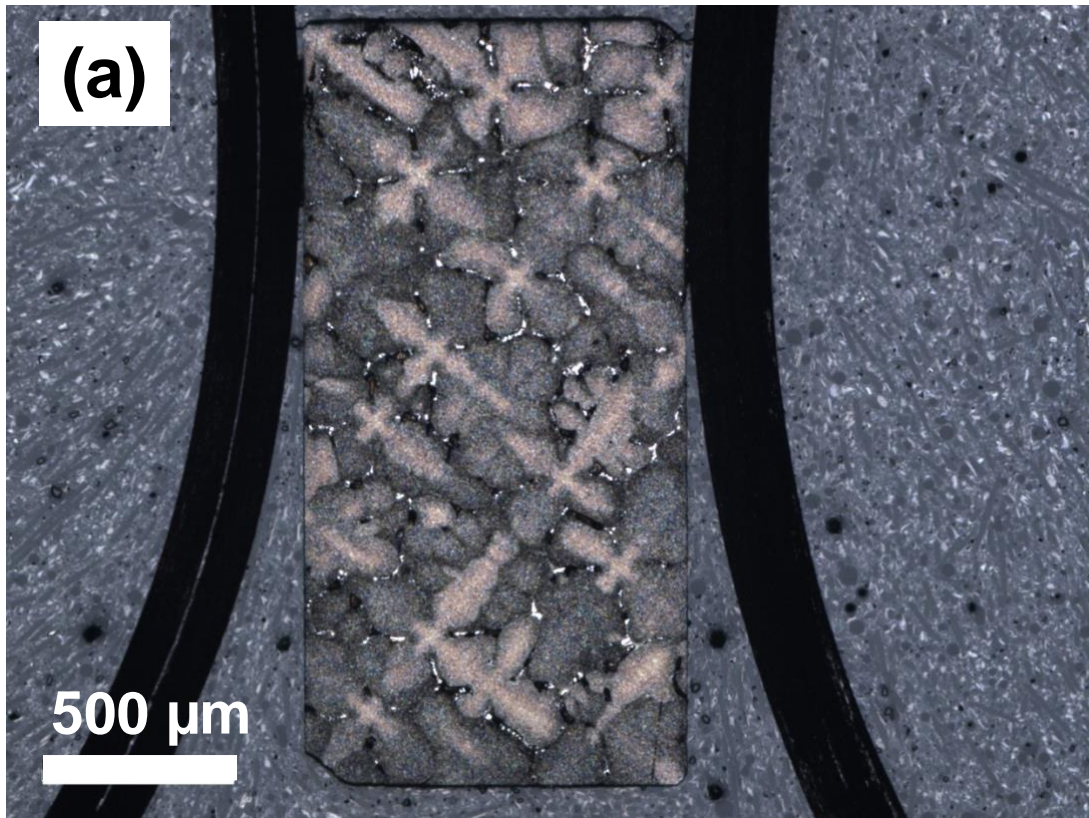


Fig. 8: Optical micrographs of transverse sections near water-cooled grip ends of ETMT for different sample cross-sections; (a) 2 mm \times 1 mm, (b) 2 mm \times 2 mm.

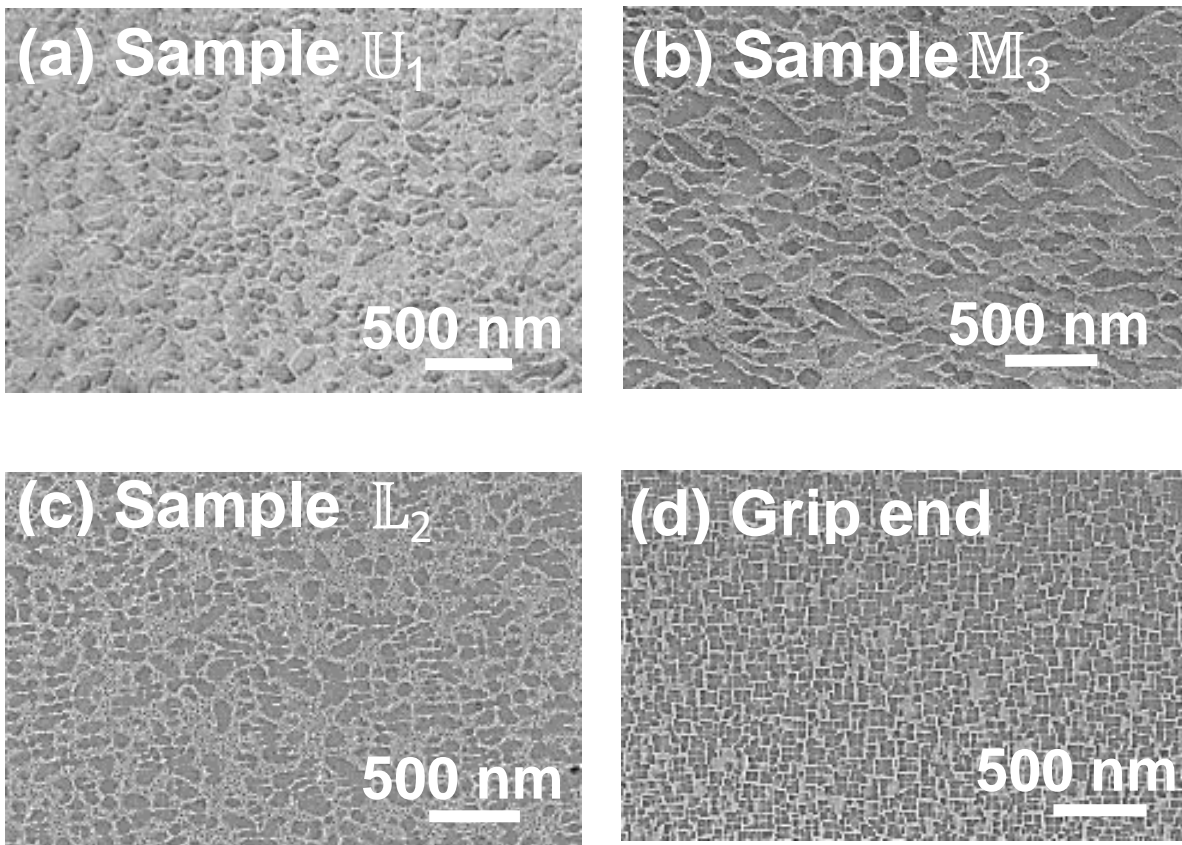


Fig. 9: Back-scattered electron images (BEI's) from continuous cooled samples within specimen gauge length and at water-cooled grip end following deformation spanning normalised resistance sub-bands; (a) sample U_1 – uppermost sub-band, (b) sample M_3 – middle sub-band, (c) sample L_2 – lowermost sub-band, (d) water-cooled grip end.

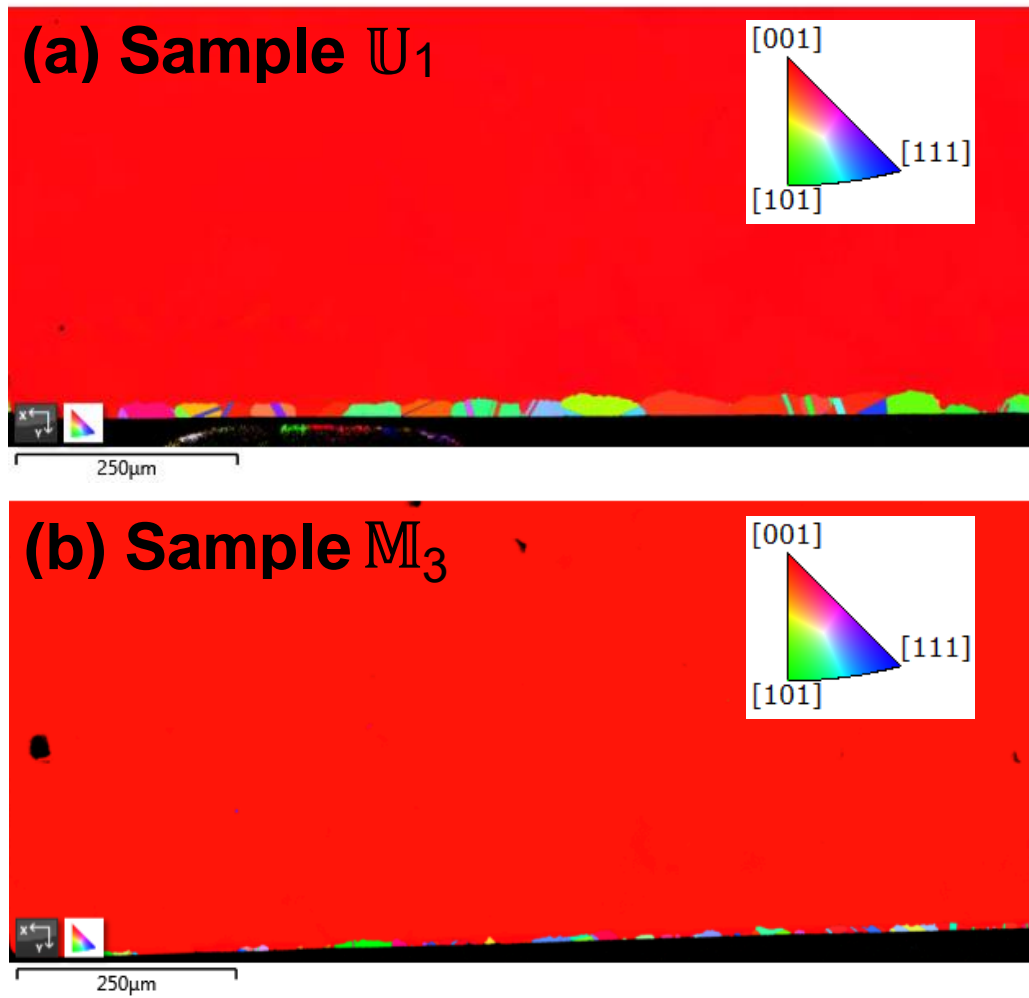


Fig. 10: Electron back-scattered diffraction from continuous cooled samples within specimen gauge length following deformation and spanning normalised resistance sub-bands. Band contrast and inverse pole figures (IPF's) from (a) sample U_1 – uppermost sub-band, and (b) sample M_3 – middle sub-band.

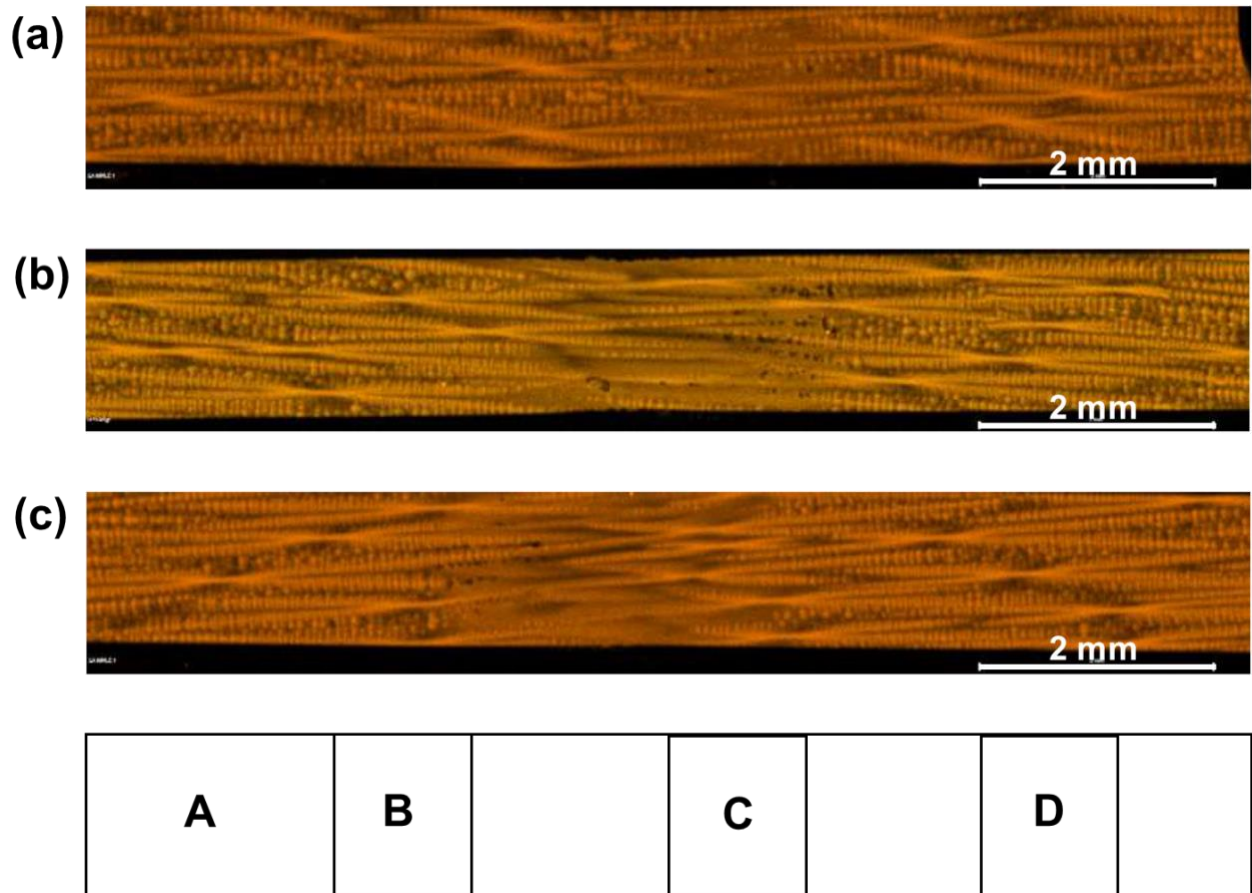


Fig. 11: Re map using Micro X-ray fluorescence along the gauge length in the as-cast cooling experiments; (a) sample U_1 , (b) sample M_3 , (c) sample L_2 .

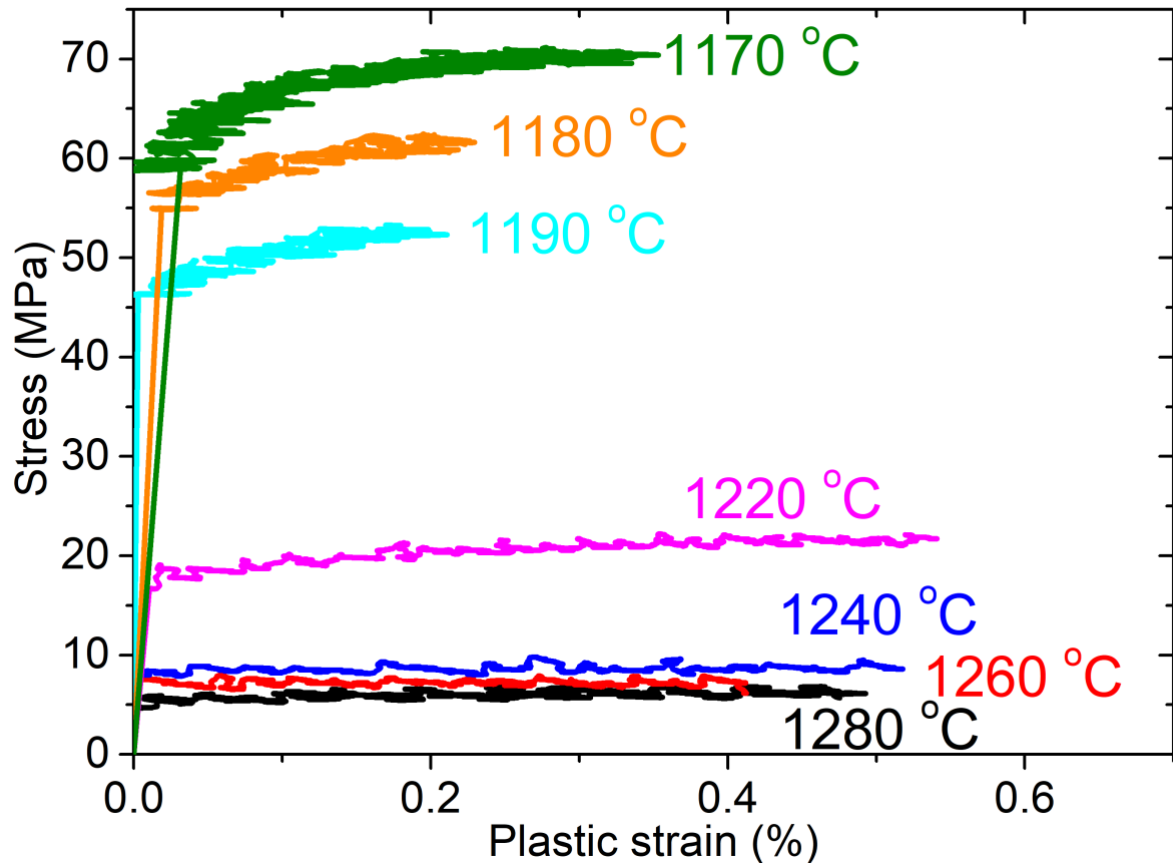


Fig. 12: Variation in flow stress with plastic strain corresponding to 1280°C, 1260°C, 1240°C and 1220°C for sample F_1 , as well as at 1190°C, 1180°C and 1170°C for sample F_2 .

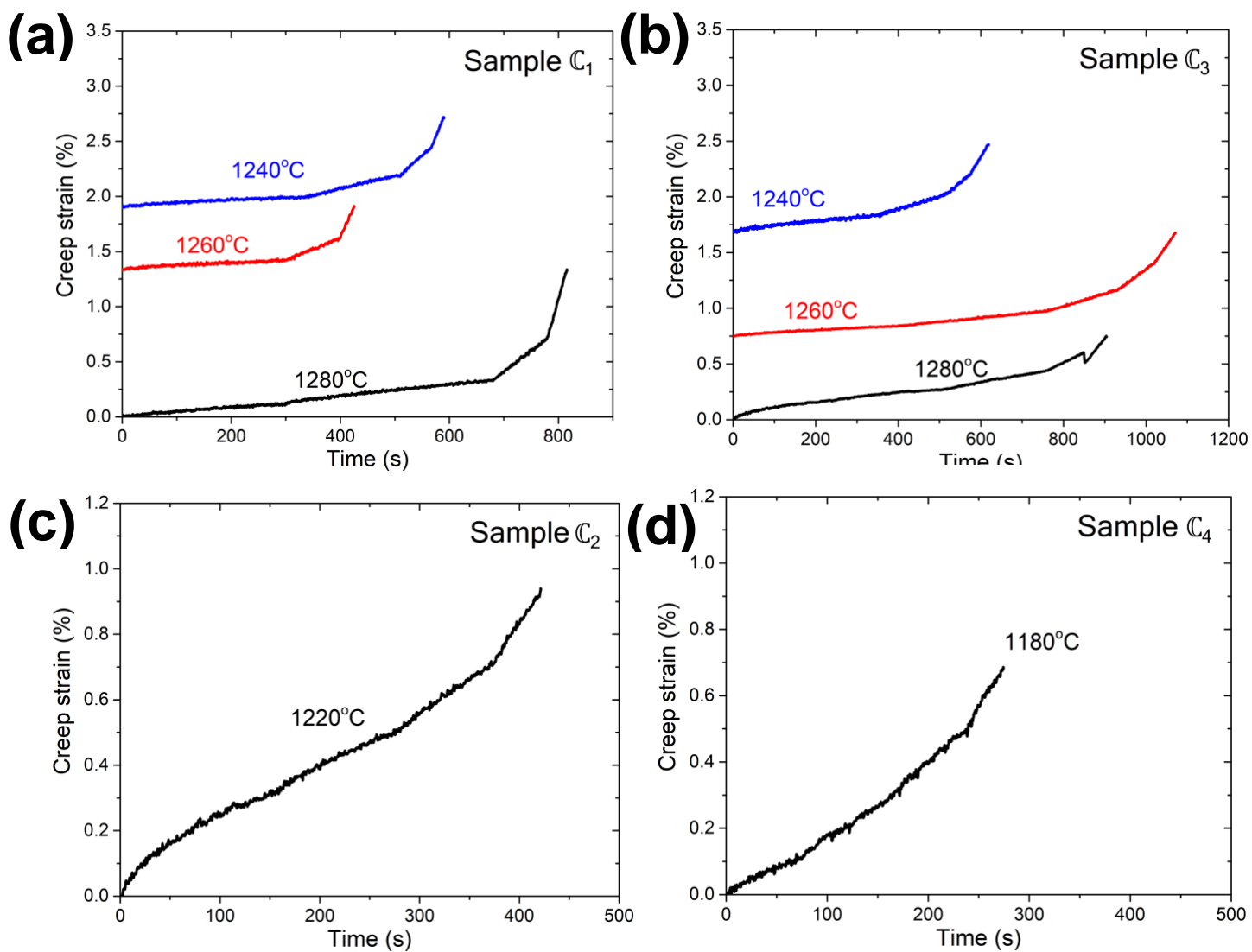


Fig. 13: Variation of creep strain with stress at different temperatures; (a) and (b) 1280°C, 1260°C and 1240°C for samples C_1 and C_3 respectively using method 1, (c) and (d) 1200°C and 1180°C for samples C_2 and C_4 respectively using method 2.

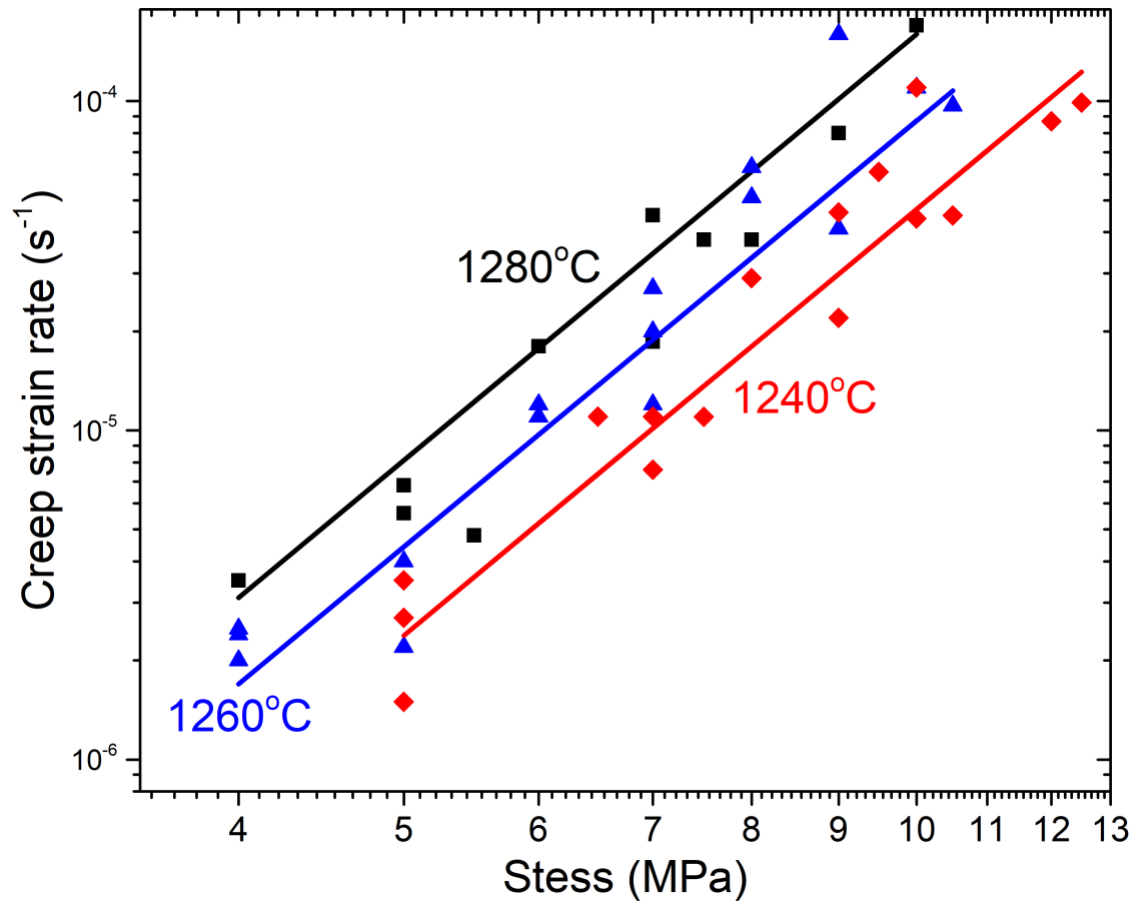


Fig. 14: Steady-state creep rate versus stress at 1280°C, 1260°C and 1240°C.

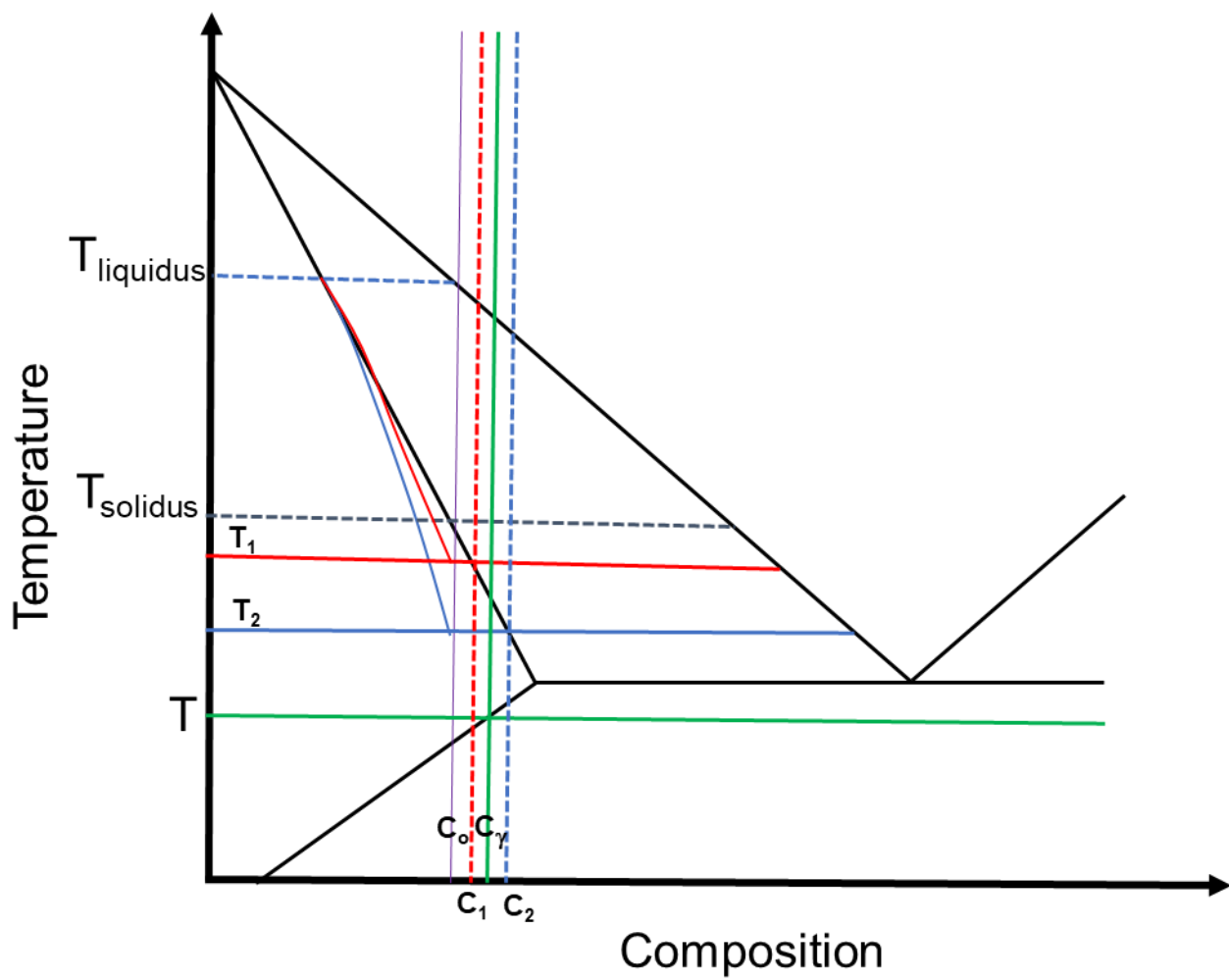


Fig. 15: Schematic illustration of the role of solidification path on the range of solvus temperatures in a binary system.

Table 1: Nominal compositions (wt. %) of CMSX4 single-crystal superalloy.

Cr	Co	Mo	Re	W	Al	Ti	Ta	Hf	Ni
6.5	9	0.6	3	6	5.6	1	6.5	0.1	Balance

Table 2: Termination of γ' dissolution during heating and onset of precipitation during cooling under zero-load for near-solutioned samples; S_1 , S_2 and S_3 .

Sample (near-solutioned)	Zero Load – Dissolution and Precipitation of γ'		Continuous Cooling – Onset of Hardening		
	End - Heating Curve	Onset - Cooling Curve	Onset Temperature	Stress (MPa)	Plastic Strain (%)
S_1	1292°C	1274°C	1260°C	13.1	0.98
S_2	1259°C	1251°C	1230°C	12.2	1.63
S_3	1283°C	1265°C	1250°C	12.7	1.10

Table 3: The two temperature regimes in the evolution of stress delineating the onset of hardening in the cooling experiments under displacement control, in the as-cast condition.

Sample (as-cast)	Continuous Cooling – Onset of Hardening		
	Onset Temperature	Stress (MPa)	Plastic Strain (%)
U_1, U_2	1230°C	9.6 – 12.3	1.0 – 2.0
M_1, M_2, M_3	1210°C to 1200°C	10.1 – 11.8	1.6 – 2.4
L_1, L_2	1200°C	12.1 – 12.6	1.5 – 4.9

Table 4: Elemental concentrations in wt. % of Cr, Ta and Re along regions within the gauge length using Micro X-ray fluorescence corresponding to as-cast cooling experiments samples U_1 , M_3 and L_2 .

Sample U_1			Sample L_2			Sample M_3		
Cr	Ta	Re	Cr	Ta	Re	Cr	Ta	Re
5.71 ± 0.01	6.18 ± 0.04	1.93 ± 0.02	5.72 ± 0.01	6.14 ± 0.11	2.00 ± 0.11	5.72 ± 0.03	6.38 ± 0.40	1.93 ± 0.06

Table 5: Saturation stress and plastic strain at 1280°C, 1260°C, 1240°C and 1220°C in the flow stress experiments for sample F_1 , as well as at 1190°C, 1180°C and 1170°C for sample F_2 . The strain is cumulative, and the amount imparted at the given temperature is underlined. Also included is the corresponding stress and strain at those temperatures in the cooling experiments (U_1 and U_2), having normalised resistance in the uppermost sub-band.

Sample	Stress (MPa) and Plastic Strain (%) - Uppermost sub-band of Normalised Resistance							
	1280°C		1260°C		1240°C		1220°C	
	ϵ (%)	σ (MPa)	ϵ (%)	σ (MPa)	ϵ (%)	σ (MPa)	ϵ (%)	σ (MPa)
F_1 (flow stress)	<u>0.56</u>	6.5	<u>1.08</u>	7.5	<u>1.70</u>	9.5	<u>2.49</u>	22.5
U_1 (cooling)	0.47	6.7	0.80	8.1	1.03	9.6	1.57	22.2
U_2 (cooling)	0.83	7.6	1.46	9.1	2.03	12.3	2.86	26.9
	Stress (MPa) and Plastic Strain (%) - Uppermost sub-band of Normalised Resistance							
	1190°C		1180°C		1170°C			
	ϵ (%)	σ (MPa)	ϵ (%)	σ (MPa)	ϵ (%)	σ (MPa)		
F_2 (flow stress)	<u>1.76</u>	52	<u>1.99</u>	61	<u>2.34</u>	70		
U_1 (cooling)	2.4	53.8	2.5	65.5	2.7	75.7		
U_2 (cooling)	4.05	62	4.37	72.5	4.64	83.5		

Table 6: Creep experiments at 1280°C, 1260°C and 1240°C corresponding to samples C_1 and C_3 having normalised resistance in the uppermost and middle sub-band using Method 1. Creep experiments at 1220°C and

1180°C corresponding to samples C₂ and C₄ respectively having normalised resistance in the uppermost using Method 2. The strain is cumulative, and the amount imparted at the given temperature is underlined.

Creep Experiments at different Temperatures, Stress (MPa), Strain (%) and Strain Rate (s⁻¹) – Uppermost sub-band of Normalised Resistance								
1280°C - C₁			1260°C - C₁			1240°C - C₁		
σ (MPa)	ε (%)	ε̇ (× 10⁻⁵ s⁻¹)	σ (MPa)	ε (%)	ε̇ (× 10⁻⁵ s⁻¹)	σ (MPa)	ε (%)	ε̇ (× 10⁻⁵ s⁻¹)
3	<u>0.11</u>	0.4	4	1.42	0.2	5	1.98	0.15
5	0.32	0.56	7	1.63	2.0	7.5	2.18	1.1
7.5	0.70	3.8	10	1.91	11.0	10	2.41	4.4
10	1.34	17.0	-	-	-	12.5	2.72	9.9
1280°C - C₃			1260°C - C₃			1240°C - C₃		
σ (MPa)	ε (%)	ε̇ (× 10⁻⁵ s⁻¹)	σ (MPa)	ε (%)	ε̇ (× 10⁻⁵ s⁻¹)	σ (MPa)	ε (%)	ε̇ (× 10⁻⁵ s⁻¹)
4	<u>0.25</u>	0.35	4	0.84	0.24	5	1.77	0.35
5	0.27	0.68	5	0.97	0.40	6.5	2.0	1.1
6	0.43	1.8	6	1.16	1.1	8	2.20	2.9
7	0.74	4.5	7	1.39	2.7	9.5	2.46	6.1
-	-	-	8	1.68	5.1	-	-	-
1220°C - C₂			1180°C - C₄					
σ (MPa)	ε (%)	ε̇ (× 10⁻⁵ s⁻¹)	σ (MPa)	ε (%)	ε̇ (× 10⁻⁵ s⁻¹)			
28	1.87	1.8	70	2.43	1.5			
30	2.01	1.4	74	2.53	2.0			
32	2.23	2.1	78	2.67	2.7			
35	2.45	4.5	83	2.87	4.8			